博士論文

First principles study on electrocatalyst/water interfaces for oxygen reduction/evolution reactions

（第一原理計算に基づく酸素還元/酸素生成反応の電極触媒/水界面に関する研究）

渡部絵里子

Preface

This thesis is based on research for electrocatalyst/water interfaces for oxygen reduction and evolution reactions under the supervision of Professor Koichi Yamashita and Associate Professor Hiroshi Ushiyama.

First, I would like to express the deepest appreciation to my supervisor Professor Koichi Yamashita, who first leaded me to the research field of *theoretical chemistry*. I would like to thank him for the excellent supervision and the encouragement throughout the six years since I joined Yamashita-Ushiyama group.

I would also like to thank Associate Professor Hiroshi Ushiyama for everyday discussion and studies on electrochemistry and catalysis. His tremendous support has been enormous help for me.

Secondly, I would like to thank staffs in Yamashita-Ushiyama group. Dr. Mikiya Fujii have provided me valuable advice on research and taught me the management of computer system. Ms. Mayumi Iyama and Ms. Noriko Sanpei have been supportive about the administration issues.

I would like to express my profound gratitude to Professor Jan Rossmeisl who allowed me to visit his group in Technical University of Denmark. I have a vivid memory of happy days in Denmark. It was absolutely wonderful and unforgettable. Through the collaborative work with Jan, we have shared deep interest in electrochemistry. I also want to thank Dr. Mårten E. Björketun. I have learnt about electrochemical interface from him which have greatly improved my researches.

I also want to thank student members and alumni in the group. Special thanks to the members of catalyst group who has been sharing interest in chemical reactions. Discussion with Mr. Rinpei Kindaichi has deepened my understanding of catalysis. Studying with Mr. Noriki Mizukimi, Mr. Rinpei Kindaichi, Mr. Tomoshi Imamura and Mr. Soichiro Ishida has been enjoyable time and broadened my horizon.

I specially wish to thank former members in Yamashita-Ushiyama group. I would like to thank Dr. Ryota Jono. I have received a lot of advice and comments from him including programming technics and attitude about science. Everyday discussion and collaborative work with him has been valuable for studying solar cells and molecular science. Dr. Tatsuhiko Ohto gives me insightful comments and advice on research. Dr. Ayaka Kuroki has been one of the kindest person. I would like to express my heartfelt gratitude to her. I also want to thank Dr. Hiroki Kawai. I receive considerable encouragement and help from him and regularly discussion with him has stimulate my motivation for studying.

Finally, I would like to express my cordial gratitude to my family. With their sincere encouragement, I manage to carry out my PhD thesis.

Eriko Watanabe

January 2016

Table of Contents

Chapter 1

General Introduction

Hydrogen energy is abstracting many interests as an alternative system for fossil fuel. Hydrogen production by splitting water with photo(electro)chemical system and power generation from hydrogen as clean energy resource are sustainable ways to utilize solar energy in electricity. I first briefly mention about basics of polymer electrolyte fuel cell (PEFC) and water-splitting system following to ref 1-3. Figure 1-1 illustrates PEFC and photoelectrochemical (PEC) water-splitting system.

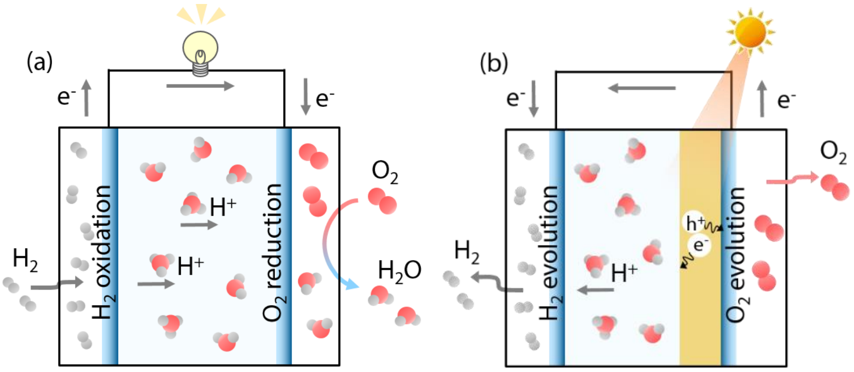

Figure 1-1. Schematic representation of (a) fuel cell and (b) photoelectrochemical water-splitting.

In PEFC, hydrogen oxidation and oxygen reduction proceed to generates water.

Cathode reaction: $O_2 + 4H^+ + 4e^- \rightarrow 2H_2O$ (R1)

Anode reaction: $H_2 \rightarrow 2H^+ + 2e^-$ (R2)

Ideally, the chemical energy by the reactions i.e. ΔG^0=-237.13 kJ/mol is converted into electric energy with equilibrium potential of 1.23 V. However, practical potential differs from the thermodynamic value of 1.23 V. The overpotential in PEFC originates from activation losses, Ohmic losses and mass transport losses. Among them, sluggish kinetics of oxygen reduction reaction (ORR) at cathode is a major cause for overpotential. To lower the overpotential, Pt-based catalysts are mainly used for ORR.

On the other hand, in electrochemical water-splitting system, cathode and anode reactions are the reverse of PEFC anode and cathode reactions, which also proceed with equilibrium potential of 1.23 V in thermodynamic limit,

Cathode reaction: $2H^+ + 2e^- \rightarrow H_2$ (R3)

Anode reaction: $2H_2O \rightarrow O_2 + 4H^+ + 4e^-$. (R4)

To utilize solar power as an energy source for the reaction, electrochemical system is combined with solar cell, photocatalyst or photoelectrode. In photo(electro)catalysts, excited charge carrier (electrons and holes) generated by photo absorption of semiconductor can split the water into hydrogen and oxygen. Similar to PEFC, oxygen evolution reaction (OER) at anodes in PEC water-splitting has the non-zero overpotential and electrocatalysts are used for OER. From benchmark experiments, even RuO_2 or IrO_2, one of the most active electrocatalysts, has the overpotential of 0.25 V.[4] To reduce the overpotential of ORR and OER, highly active electrocatalysts are strongly desired.

The ORR and OER are reverse reactions each other, and have the similar reaction coordinate in ground state. In the search for ORR/OER electrocatalysts with low overpotential, thermodynamic guidelines have been proposed. For example, Fernández et al provided a guideline for the design of bimetallic electrocatalysts.[5] They showed coupling a good O-O bond cleaving metal and a good oxygen reducing metal can improve ORR activity by using scanning electrochemical microscopy. Nørskov et al examined ORR activities on various metals and clearly showed volcano-shaped relationship between activity and oxygen binding energy by using a pioneering method for calculating electrochemical reactions.[6] Rossmeisl et al also showed volcano-shaped relationship for OER on oxide surfaces.[7] In their study, four elementary reactions are assumed for ORR as follows

$$O_2 + H^+ + e^- \rightarrow OOH^* \qquad \text{(R5)}$$

$$OOH^* + H^+ + e^- \rightarrow H_2O + O^* \qquad \text{(R6)}$$

$$O^* + H^+ + e^- \rightarrow OH^* \qquad \text{(R7)}$$

$$OH^* + H^+ + e^- \rightarrow H_2O \qquad \text{(R8)}$$

where proton coupled electron transfer is assumed on every step. Additionally, they found an internal relationship among binding energies of O*, OH* and OOH*. The internal relationship enables us to reduce the number of variables as descriptors of catalytic activity; the catalytic activity can be tuned by a single descriptor - the oxygen binding energy. Along with the guideline of finding the catalyst at the top of volcano, great success has been achieved in ORR and OER catalysts with experimental evidence.[8-10] The simple guideline has established and been supplying preliminary understandings for ORR and OER.

The guideline can also bridge ORR/OER activity and basic fundamental science.[11] The universal volcano-shaped relationship is related to Sabatier's principle, the old and fundamental concept for catalysis. It says that, in general, the adsorption strength and catalytic activities have the volcano-shaped relationship, that is, catalysts have maximum activity when the binding energy of the reactant is neither too weak nor too strong. It implies that the strength of the surface–reactant interaction can be a descriptor for optimizing the catalytic activity. From Hoffmann's model, the strength of the interaction is dominated by the energy level of molecular orbital and the metal density of states. Therefore, in case of metal catalysis, position of metal *d* band is the main descriptor for the catalytic activity. Figure 1-2 shows the transition of theory for catalysis from the qualitative one in 1970s to the qualitative understanding in early 2000s. Theories for chemical bonding and catalytic activity in 1970s are very well confirmed as *d*-band model and volcano relationship by means of DFT calculations. The connection between catalytic activity and fundamental concept of surface-reactant interactions opens up a way of computational design of catalysts.

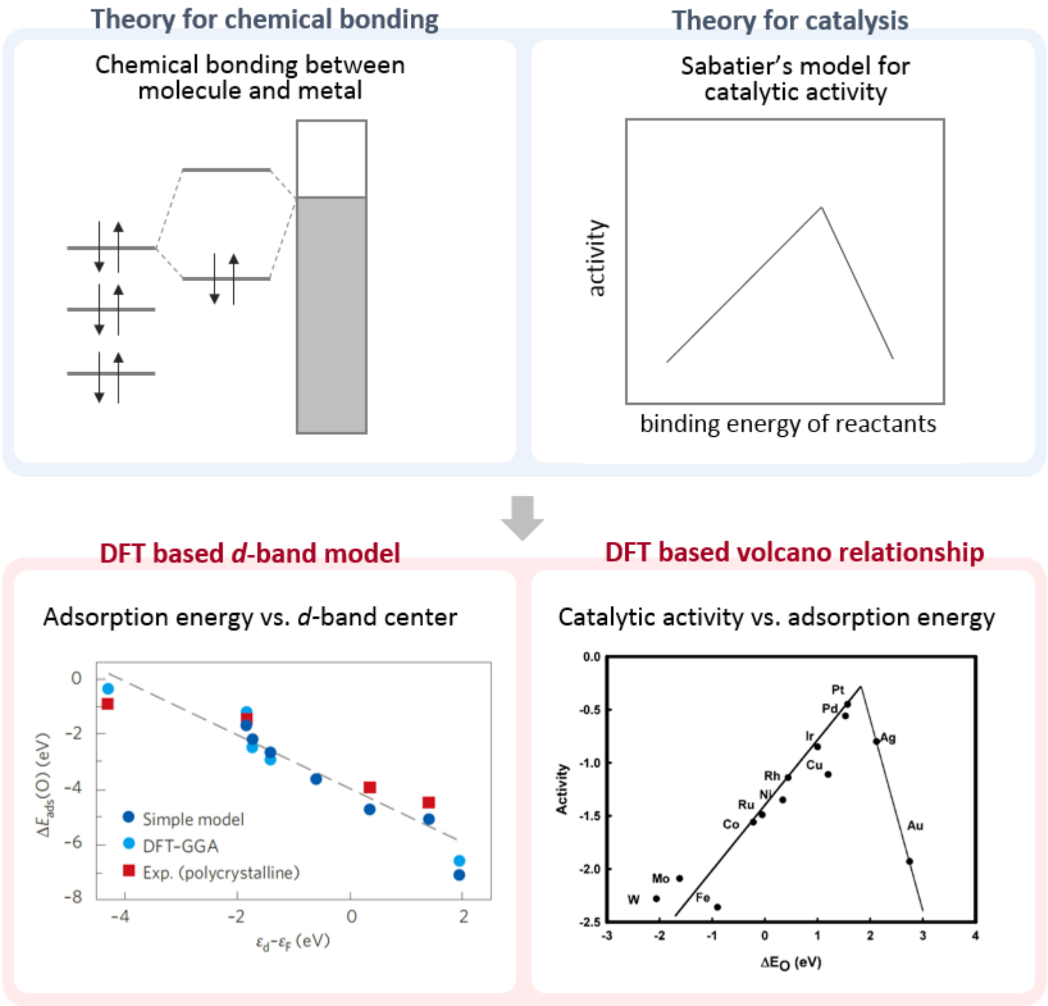

Figure 1-2. Connection between theories in 1970s and DFT calculations in early 2000s. Left part; theory for chemical bonding. The primary model for the bonding between reactant and metal surface is first addressed by R. Hoffmann in ref. 12. Later the theory is confirmed by *d*-band model (adapted from ref. 13). Right part; theory for optimizing catalyst. The primary model was first suggested by Sabatier and later, it is confirmed in DFT based volcano-relationship (adapted from ref. 6).

Apart from the great success of finding an “optimal catalyst”, finding the “ideal” catalyst that has zero overpotential has not been achieved; we have to overcome at least three challenges. The first challenge is an existence of the thermodynamic limit. The limit is discussed by Koper, addressing that even the “best” catalyst has non-zero overpotential on metal (111) surfaces because interdependence of binding energies of O, OH and OOH limits the degree of freedom.[14] According to the previous study, adsorption energies of OH, O and OOH have their optimal values of 1.23 eV, 2.46 eV and 3.69 eV respectively, where thermodynamic overpotential of each elementary step becomes zero.[6] However, the interdependence found on metal (111) surfaces

$$\Delta G(\mathrm{OH_{ads}}) \approx 0.50 \times \Delta G(\mathrm{O_{ads}}) + 0.04\ \mathrm{eV}$$

$$\Delta G(\mathrm{OOH_{ads}}) \approx 0.53 \times \Delta G(\mathrm{O_{ads}}) + 3.33\ \mathrm{eV}$$

always give rise to the fixed binding energy difference of approximately 3.29 eV between adsorption energies of OH and OOH. Thus, it is impossible to set the binding energies of O, OH and OOH to their optimal values at a time. Such interdependencies have been verified on metals and oxides,[7,15] and finding ORR/OER electrocatalysts with low overpotential has been suffering from them. One potential approach to break the interdependence is local active site modifications. For example, doping metals in metal oxide[16], and confinement of active site in three dimensional channel[17] are suggested to break the scaling relationship. The local characters such as impurities, surface poisoning and surface oxidation/reduction can be, whether good or bad, the cause for either increased or decreased activity. More complicated surface models with impurities and defects should be discussed to provide the efficient ORR/OER electrocatalysts.

The second challenge is to address an electron/hole transfer across the electrocatalyst/water interface. Most electrochemical reactions based on DFT with periodic boundary condition handle thermodynamics of H^+ and e^- at the same time. However, it is well-known that the interfaces of electrocatalyst/water form either Schottky or Ohmic junction, which strongly affect the thermodynamics of electron and hole transfers. In PEFC, overpotential for ORR can be caused by the formation of Schottky barrier because it prevents electron transfer from the electrocatalyst to water. In the case of OER in PEC water-splitting system, the formation of Schottky barrier is favorable because it accelerates the hole transfer from the electrocatalyst to water. Insights into interfaces from the viewpoint of the types of junctions (Schottky of Ohmic) and magnitude of them are of critical importance, however most of theoretical studies have not payed attention to them.

The third challenge is to bridge the simulation model and experimental environment. It is observed that the maximum activity in experiments cannot reach to their theoretical predictions.[15] Most theoretical studies are based on highly idealized situations; yet, surface porosity, roughness, corrosion, defect, and other features are, somewhat inevitable in electrochemical environment and significantly change the activity. Furthermore, despite the fact that electrochemical environment is extremely complex where electrode potential, solvent, pH, and electric field are involved, effects of the electrolyte, pH and electric field are often neglected in the simulations. Essentially, these should be addressed because the activity of real electrocatalyst is highly dependent on electrochemical condition. An atomic-scale analysis of materials in electrochemical condition possibly maximizes the potential of materials. Schemes to approach electrochemical reaction by density functional theory will be reviewed in Chapter 2.

In this thesis, my goal is overcoming aforementioned challenges to uncover the interfacial structures and reactions of ORR and OER. In Chapter 2, a brief introduction to the density functional theory and theoretical treatment of electrochemical reaction are given. In Chapter 3, the reaction mechanism of oxygen reduction on Ta_3N_5(100) is examined as Pt-free electrocatalyst. Especially, the role of impurity is focused throughout the Chapter. By introducing simple substitutions of O atom to N atom, it is shown that the activity of surfaces with and without impurities are quite different and impurities have a positive effect on lowering overpotential. In Chapter 4, structures and band alignment of an n-type Ta_3N_5/water interface at given electrode potential are discussed. In addition to introducing impurities, more complicated models are employed in this Chapter; aqueous environment with variety of charges at the interface are introduced to mimic the electrochemical environment. Calculations on such models can reveal a band diagram at the interface under given electrode potentials. It is shown that Schottky barrier height is depending on the electrode potential and significance of surface states and surface modification is found. In Chapter 5, more sophisticated method are employed for an analysis of atomic-scale interface of the RuO_2/water under electrochemical environment. An Effect of pH is addressed together with electrode potential and electric field. As a result, the considerable difference of interfacial structures at pH 0 and 14 can be found for the first time. In Chapter 6 I conclude with some remarks.

References

(1) S. J. Paddison, K. S. Promislow, Device and Materials Modeling in PEM Fuel Cells, 2009, Splinger

(2) A. Wieckowski, J. K. Nøorskov, Fuel Cell Science Theory, Fundamentals, and Biocatalysis, 2010, Wiley

(3) M. G. Walter, E. L. Warren, J. R. McKone, S. W. Boettcher, Q. Mi, E. a. Santori and N. S. Lewis, *Chem. Rev*., 2010, **110**, 6446.

(4) C. C. L. McCrory, S. Jung, J. C. Peters and T. F. Jaramillo, *J. Am. Chem. Soc*., 2013, **135**, 16977.

(5) J. L. Fernández, D. a Walsh and A. J. Bard, *J. Am. Chem. Soc*., 2005, **127**, 357.

(6) J. K. Nørskov, J. Rossmeisl, A. Logadottir, L. Lindqvist, J. R. Kitchin, T. Bligaard and H. Jónsson, *J. Phys. Chem. B*, 2004, **108**, 17886.

(7) I. C. Man, H.-Y. Su, F. Calle-Vallejo, H. a. Hansen, J. I. Martínez, N. G. Inoglu, J. Kitchin, T. F. Jaramillo, J. K. Nørskov and J. Rossmeisl, *ChemCatChem*, 2011, **3**, 1159.

(8) J. Greeley, I. E. L. Stephens, A. S. Bondarenko, T. P. Johansson, H. A. Hansen, T. F. Jaramillo, J. Rossmeisl, I. Chorkendorff and J. K. Nørskov, *Nat. Chem*., 2009, **1**, 552.

(9) V. R. Stamenkovic, B. S. Mun, M. Arenz, K. J. J. Mayrhofer, C. a Lucas, G. Wang, P. N. Ross and N. M. Markovic, *Nat. Mater*., 2007, **6**, 241.

(10) J. Suntivich, H. A. Gasteiger, N. Yabuuchi, H. Nakanishi, J. B. Goodenough and Y. Shao-Horn, *Nat. Chem*., 2011, **3**, 546.

(11) A. Nilsson, L. G. M. Pettersson, J. K. Nørskov, Chemical Bonding at Surface and Interfaces, 2008, Elsevier

(12) R. Hoffmann, *Rev. Mod. Phys*., 1988, **60**, 601

(13) J. K. Nørskov, T. Bligaard, J. Rossmeisl, C. H. Christensen, *Nat. Chem*., 2009, **1**, 37

(14) M. T. M. Koper, *J. Electroanal. Chem*., 2011, **660**, 254.

(15) I. E. L. Stephens, A. S. Bondarenko, U. Grønbjerg, J. Rossmeisl, I. Chorkendorff, *Energy Environ. Sci*., 2012, **5**, 6744.

(16) N. B. Halck, V. Petrykin, P. Krtil and J. Rossmeisl, *Phys. Chem. Chem. Phys*., 2014, **16**, 13682.

(17) A. Doyle, J. Montoya, and A. Vojvodic, *ChemCatChem*, 2015, **7**, 738.

Chapter 2

Theoretical Background

2.1 **Density Functional Theory**

In this part, density functional theory is introduced following to ref 1 and 2. DFT is one of the most frequently used method that can handle many-body system with correlations. By approximating interactions between particles with correlations to those of independent particles, DFT can be well applied in a field of materials science. DFT is based on Hohenberg-Kohn theorem that proves the possibility of electronic density as a unique descriptor for external potentials. Later in 1964, Kohn and Sham proposed the concrete equation that can be computationally solved by approximating the many-body effect into exchange-correlation term in Kohn-Sham equations. Here, we start from Schrodinger equations and then Hohenberg-Kohn theorm and Kohn-Sham equations are introduced.

2.1.1 Hamiltonian

A Hamiltonian of system including the interaction between electrons and nucleus can be represented regardless of molecules and solids as

$$\begin{aligned}\widehat{H} = \sum\nolimits_{I=1}^{P} \frac{\hbar^2}{2M_I}\nabla_I^2 - \sum\nolimits_{i=1}^{N} \frac{\hbar^2}{2m}\nabla_i^2 + \frac{e^2}{2}\sum\nolimits_{I=1}^{P}\sum\nolimits_{J\neq I}^{P} \frac{Z_I Z_J}{\left|\mathbf{R}_I - \mathbf{R}_J\right|} \\ + \frac{e^2}{2}\sum\nolimits_{i=1}^{N}\sum\nolimits_{j\neq i}^{N} \frac{1}{\mathbf{r}_i\mathbf{r}_j} \\ - e^2\sum\nolimits_{I=1}^{P}\sum\nolimits_{i=1}^{N} \frac{Z_I}{\left|\mathbf{R}_I - \mathbf{r}_i\right|}\end{aligned} \tag{2.1}$$

where $\mathbf{R} = \{\mathbf{R}_I\}$, $\mathrm{I} = 1\sim P$ are coordinates of P number of nucleus, $\mathbf{r} = \{\mathbf{r}_i\}$, $i = 1\sim N$ are coordinates of N number of electrons, M_I is a mass of nucleus I, m is a mass of electron and Z_I is a charge of nucleus I respectively. First and second terms are kinetic energy of the nuclei and electrons. The other term is the electrostatic interaction of nuclei-nuclei, electron-electron, and nuclei-electron, respectively. For here on, atomic unit (a. u.) is used in brevity. In principle, electronic states can be obtained by solving Schrodinger equation

$$\widehat{H}\Psi_i(\mathbf{r},\mathbf{R}) = E_i\Psi_i(\mathbf{r},\mathbf{R}). \tag{2.2}$$

However, analytical or numerical solution of Schrodinger equation is limited to only a few cases. Born-Oppenheimer approximation is a first step in solving Schrodinger equation with reasonable accuracy. Because of 10^3 to 10^5 mass difference in nuclei and electron, the motion of nuclei and electron can be separated. Under this approximation, electrons stay their stationary point defined by electronic Hamiltonian,

$$\widehat{H}_{el} = \widehat{T} + \widehat{V}_{ext} + \widehat{U}_{ee} + E_{II} \tag{2.3}$$

where first, second and third terms represent the kinetic energy of electron, potential from nuclei and electron-electron interaction respectively,

$$\hat{T} = -\sum_i \nabla_i^2 \tag{2.4}$$

$$\hat{V}_{ext} = \sum_{i,I} \frac{Z_I}{|\mathbf{r}_i - \mathbf{R}_I|} \tag{2.5}$$

$$\hat{U}_{ee} = \frac{1}{2}\sum_{i\neq j} \frac{1}{|\mathbf{r}_i - \mathbf{r}_j|}. \tag{2.6}$$

The last term is nuclei-nuclei interaction and should be constant when the coordinates of nucleus are fixed. Thus, the total energy of the ground state consisting of N electrons under Born-Oppenheimer approximation is

$$E = \langle\Phi|\hat{T}|\Phi\rangle + \langle\Phi|\hat{V}_{ext}|\Phi\rangle + \langle\Phi|\hat{U}_{ee}|\Phi\rangle + E_{II} \tag{2.7}$$

where Φ is N-electron ground density wave function of the system including all the effect such as electron correlation. The remaining part of nuclei motion is often solved with classical equation

$$M_I \frac{\partial^2}{\partial t^2}\mathbf{R}_\mathrm{I} = -\frac{\partial E}{\partial \mathbf{R}_I}. \tag{2.8}$$

The force acting on atoms can be described by Hellmann-Feynman force

$$-\frac{\partial E}{\partial \mathbf{R}_I} = -\frac{\partial}{\partial \mathbf{R}_I}\langle\Phi|\hat{H}_{el}|\Phi\rangle = -\left\langle\Phi\left|\frac{\partial \hat{H}_{el}}{\partial \mathbf{R}_i}\right|\Phi\right\rangle. \tag{2.9}$$

2.1.2 Hohenberg-Kohn theorem

Density functional theory is electron density based method. An idea to express the energy in terms of density is first proposed by Thomas and Fermi prior to Hohenberg-Kohn theorem. They formulated the total energy as a function of homogeneous electron gas density. Later, Hohenberg and Kohn proved that the whole system can be purely described by the electron density of the ground state. Hohenberg-Kohn theorm can be divided in two.

theorem I:

Ground state density of a system of interacting electrons in an external potential $\hat{V}_{\mathrm{ext}}$ uniquely determines this potential except for a constant.

proof:

The proof proceeds by reduction ad absurdum. Suppose one ground state electron density $n_0(\mathbf{r})$ has two corresponding external potential $\hat{V}_{\mathrm{ext}}$ and $\hat{V'}_{\mathrm{ext}}$ which satisfies $\hat{V}_{\mathrm{ext}} - \hat{V}'_{\mathrm{ext}} = const.$ The wave function and total energy associated with $\hat{V}_{\mathrm{ext}}$ is Ψ and $E_0 = \langle \Psi | \hat{H} | \Psi \rangle$ and those with $\hat{V'}_{\mathrm{ext}}$ is Ψ' and $E'_0 = \langle \Psi' | \hat{H'} | \Psi' \rangle$. With variation principles, we can obtain the inequality by taking Ψ' as trial wave function,

$$\begin{aligned} E_0 &< \langle \Psi' | \hat{H} | \Psi' \rangle = \langle \Psi' | \hat{H'} | \Psi' \rangle + \langle \Psi' | \hat{H} - \hat{H'} | \Psi' \rangle \\ &= E'_0 + \langle \Psi' | \hat{V}_{\mathrm{ext}} - \hat{V'}_{\mathrm{ext}} | \Psi' \rangle. \end{aligned} \tag{2.10}$$

Similarly, by interchanging prime and unprimed in (2.10),

$$E'_0 < E_0 + \langle \Psi | \hat{V'}_{\mathrm{ext}} - \hat{V}_{\mathrm{ext}} | \Psi \rangle \tag{2.11}$$

is obtained. Here, an inequality of Ψ and Ψ' is used. By adding (2.10) and (2.11) each other, inconsistent formula is obtained

$$E_0 + E'_0 < E'_0 + E_0. \tag{2.12}$$

Thus, uniqueness of $n_0(\mathbf{r})$ for $\hat{V}_{\mathrm{ext}}$ is proved.

theorem II:

The total energy of the system can be described as a functional of $n(\mathbf{r})$

$$\begin{aligned} E[n] &= \langle \Psi[n] | \hat{T} + \hat{U}_{ee} + \hat{V}_{ext} | \Psi[n] \rangle \\ &= \langle \Psi[n] | \hat{T} + \hat{U}_{ee} | \Psi[n] \rangle + \int v_{ion}(\mathbf{r}) n(\mathbf{r}) d\mathbf{r} \\ &= F[n] + \int v_{ion}(\mathbf{r}) n(\mathbf{r}) d\mathbf{r}. \end{aligned} \tag{2.13}$$

Here, $F[n]$ is called 'universal functional' since it does not depend explicitly on the external potential. The exact ground state energy of the system is the global minimum value of energy functional and corresponding electron density $n(\mathbf{r})$ is exactly the density $n_0(\mathbf{r})$ of the ground state.

proof:

Given electron density $n(\mathbf{r})$, we have

$$\begin{aligned} \langle \Psi[\tilde{n}] | \hat{H} | \Psi[\tilde{n}] \rangle &= F[\tilde{n}] + \int \tilde{n}(\mathbf{r}) v_{ion}(\mathbf{r}) d\mathbf{r} \\ &= E_v[\tilde{n}] \geq E_v[n] = E_0 = \langle \Psi | \hat{H} | \Psi \rangle. \end{aligned} \tag{2.12}$$

Once $F[n]$ is provided, exact solution of ground state density and total energy can be obtained by minimizing energy of the system with respect to n.

2.1.3 **Kohn-Sham equations**

Hohenberg-Kohn theorem proves the validness of a density based method for the solution of Schrodinger equation. Soon after, Kohn and Sham proposed an idea of representing the exact ground state density by a non-interacting reference system. Hamiltonian of the non-interacting reference system is represented as follows,

$$\hat{H}_R = -\nabla^2 + v_R(\mathbf{r}). \tag{2.14}$$

The ground state energy of non-interacting reference system is equivalent to that of interacting real system. The reference system has an usual kinetic energy operator and effective local potential, which satisfies the following one-electron equation,

$$\hat{H}_R\psi_i(\mathbf{r}) = \varepsilon_i\psi_i(\mathbf{r}) \tag{2.15}$$

$$\sum_{i=1}^{N}|\psi_i(\mathbf{r})|^2 = n_0(\mathbf{r})\,. \tag{2.16}$$

The Hamiltonian does not include electron-electron interaction explicitly. An eigenvector can be represented by single Slater-determinant using one electron orbital ψ_i. Using this one electron orbital, kinetic term of non-interacting system can be written as

$$T_s[n] = -\sum_{i=1}^{N}\langle\psi_i|\nabla^2|\psi_i\rangle. \tag{2.17}$$

Also, the electron-electron interaction term is introduced similar to classical Coulomb interaction, called Hartree term,

$$E_{Hartree}[n] = \frac{1}{2}\iint\frac{n(\mathbf{r})n(\mathbf{r}')}{|\mathbf{r}-\mathbf{r}'|}d\mathbf{r}d\mathbf{r}'. \tag{2.18}$$

The kinetic term $T_s[n]$ is that of non-interacting system, and does not include the correlation effect although the real system should include. Also, the Hartree term does not include the exchange and correlation effect. The remaining part that should be included in the non-interacting system is pressed into a new term $E_{xc}[n]$ called exchange-correlation term. Then, Hohenberg-Kohn functional can be rewritten as Kohn-Sham energy functional:

$$E[n] = T_s[n] + \frac{1}{2}\iint\frac{n(\mathbf{r})n(\mathbf{r}')}{|\mathbf{r}-\mathbf{r}'|}d\mathbf{r}d\mathbf{r}' + v_{ion}(\mathbf{r})n(\mathbf{r})dr + E_{xc}[n]. \tag{2.19}$$

The unknown exchange-correlation energy E_{xc} is approximated, and will be mention in 2.1.4. Kohn-Sham equation is then introduced by Euler equation.

$$\frac{\delta}{\delta n}\left(E[n]-\mu\left[\int n(r)d\mathbf{r}-N\right]\right)=0 \tag{2.20}$$

$$\frac{\delta T_s[n]}{\delta n}+\int\frac{n(\mathbf{r}')}{|\mathbf{r}-\mathbf{r}'|}d\mathbf{r}'+v_{ion}(\mathbf{r})+\frac{\delta E_{xc}[n]}{\delta n}=\mu. \tag{2.21}$$

Here, $v_R(\mathbf{r})$ in (2.14) is defined as an effective potential of non-interacting system defined as,

$$\begin{aligned} v_R(\mathbf{r}) &= \int\frac{n(\mathbf{r}')}{|\mathbf{r}-\mathbf{r}'|}d\mathbf{r}'+v_{ion}(\mathbf{r})+\frac{\delta E_{xc}[n]}{\delta n} \\ &= v_H(\mathbf{r})+v_{ion}(\mathbf{r})+v_{xc}(\mathbf{r}). \end{aligned} \tag{2.22}$$

The first term in $v_R(\mathbf{r})$ is called 'Hartree potential' and third term is called 'exchange-correlation potential'. Finally, Kohn-Sham equation is introduced as non-interacting systems,

$$\left(-\nabla^2+v_R(\mathbf{r})\right)\psi_i(\mathbf{r})=\varepsilon_i\psi_i(\mathbf{r}). \tag{2.23}$$

Solving Kohn-Sham equation, in principle, give the exact electron density and total energy. However, the exact formula of exchange-correlation functional is unknown and approximation is still needed. As a result of dividing kinetic term and electron-electron interaction term in Hohenberg-Kohn functional, all the difficult part is summarized in $E_{xc}[n]$ in Kohn-Sham equation.

2.1.4 Exchange and correlation

The exchange-correlation terms $E_{xc}[n]$ has a formula of

$$E_{xc}[n]=\frac{1}{2}\iint\frac{n(\mathbf{r})\bar{n}_{xc}(\mathbf{r},\mathbf{r}')}{|\mathbf{r}-\mathbf{r}'|}d\mathbf{r}d\mathbf{r}' \tag{2.24}$$

where $\bar{n}_{xc}(\mathbf{r},\mathbf{r}')$ is called 'exchange-correlation hole' which is the reduced probability of finding electron at $\mathbf{r}'$ originating from self-interaction correction, Pauli exclusion principle and electron-electron repulsion. In other words, $E_{xc}[n]$ can be defined as the Coulomb interaction between electron density and exchange-correlation hole density. The exchange-correlation hole must satisfies a sum rule

$$\int \bar{n}_{xc}(\mathbf{r},\mathbf{r}')d\mathbf{r}' = \int \bar{n}_{xc}(\mathbf{r},\mathbf{r}')d\mathbf{r} = -1 \tag{2.25}$$

meaning that every electron creates one hole distributed in space. Therefore, exchange-correlation functional can be written in terms of $\bar{n}_{xc}(\mathbf{r},\mathbf{r}')$

$$E_{xc}[n] = \int d^3\mathbf{r}n(\mathbf{r})\varepsilon_{xc}[n](\mathbf{r}) \tag{2.26}$$

where $\varepsilon_{xc}[n](\mathbf{r}) = \frac{\bar{n}_{xc}(\mathbf{r},\mathbf{r}')}{|\mathbf{r}-\mathbf{r}'|}$ is exchange-correlation energy at $\mathbf{r}$.

Local density approximation (LDA) uses exchange-correlation hole from the homogeneous electron gas with local density

$$E_{xc}[n] = \int d^3\mathbf{r}n(\mathbf{r})\varepsilon_{xc}^{LDA}(n(\mathbf{r})). \tag{2.27}$$

The energy $\varepsilon_{xc}^{LDA}(n(\mathbf{r})) = \varepsilon_{X}^{LDA}(n(\mathbf{r})) + \varepsilon_{C}^{LDA}(n(\mathbf{r}))$ is a sum of exchange and correlation term which can be determined analytically and by fitting parametrically respectively.

Generalized gradient approximation is one improved approach by LDA in that inhomogeneity of the density is introduced as

$$\begin{gathered} E_{xc}[n] = \int d^3\mathbf{r}n(\mathbf{r})\varepsilon_{xc}^{GGA}(n(\mathbf{r}),\nabla n(\mathbf{r})) \\ \varepsilon_{xc}^{GGA}(n(\mathbf{r}),\nabla n(\mathbf{r})) = \varepsilon_{X}^{GGA}(n(\mathbf{r}),\nabla n(\mathbf{r})) + \varepsilon_{C}^{GGA}(n(\mathbf{r}),\nabla n(\mathbf{r})) \end{gathered} \tag{2.28}$$

where formulas of ε_{X}^{GGA} and ε_{C}^{GGA} is determined as to satisfy (2.25) and other some requirements.

2.2 Electrochemical method

Electrochemical reaction is the basis for energetic devices such as photo-semiconductor electrode, lithium-ion battery and electric double layer capacitor. Despite the long history of electrode reaction established long ago, analysis of the interfacial structure and reaction has been a challenging problem. To achieve high-performance devices which solve recent environmental and energetic issues, it is important to clarify the atomic scale behavior of the electrochemical interface. From the experiments, cyclic voltammetry, AC impedance method and chronoamperometry are frequently used method.[3] They enable to examine the electrochemical reaction by measuring the amount of charge transferred, resistance and diffusion constant, however, direct observation of microscopic phenomena cannot be obtained. Techniques such as STM can observe surface structure of the atomic level directly, but measurement in the solution is very difficult. Recently, techniques for probing electrochemical interface using X-ray is also applied. They enable to track the photo absorption/emission spectrum of selective atoms, however, it does not mean that direct observation of the interface is possible. In parallel to exhaustive challenges in experiments, first principle calculations also have come into play. Combination of experimental techniques and first principles calculations is a promising way for the atomic scale analysis. The characteristics of first-principles calculation is based on the quantum mechanics, and is suitable for the description of the interface behavior on the atomic scale. Density functional theory (DFT) is one representative method and can provide the information of one-electron orbital and total energy by solving Kohn-Sham equations. However, challenges of using DFT for electrochemistry also exist in two parts. First, electrochemical reaction is conducted under certain chemical potential; in other words, number of electrons is variable in the system which is normally unfeatured in DFT. Secondly, it is almost impossible to take into account the effect of pH and other solvation explicitly because the number of atoms in a simulation becomes too much. These problems mean the result directly obtained by DFT is not connecting to the electrochemical reactions. Toward an ‘in situ’ atomic scale analysis by DFT, there need the methods that bridge between real electrode reaction and simulation modeling of DFT. Here I review the methods to include the effect of electrode potential and pH.

2.2.1 Description of electrode potential in DFT

There are two main approaches to simulate electrochemical reaction with electrode potential. First approach is an explicit method based on a grand canonical model; Kohn-Sham equation in DFT is solved with constraints of *constant chemical potential* [Figure 2-1(a)]. It is a straightforward method in that it mimics an electrode reaction. Although it is closer to experimental condition than the second method mentioned below, the difficulty in implementation and convergence problem prevent the application for the electrochemical system. The other approach is implicit method based on a micro canonical modeling so called capacitor model; Kohn-Sham equation is solved with constraints of *constant number of electron*s [Figure 2-1(b)]. It needs some corrections to combine the effect of electrode potential. Despite a need for some corrections to combine the effect of electrode potential, large amount of works have been done along with this approach. The advantage of the method is it can be performed within the framework of normal DFT. With appropriate correction and modeling of the system, it is a powerful method for the simulation of electrochemical system.

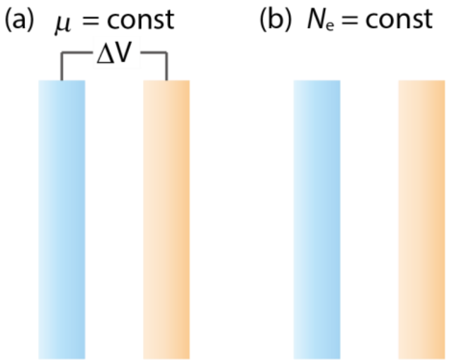

Figure 2-1 Illustration of two models for simulating electrochemical system in DFT. (a) μ=const. model (b)N_e=const. model

A. Grand canonical description; $\mu = const.$ model

A possibility for grand canonical description in DFT is based on a proof by Mermin in 1965.[4] In his work, in contrast to original DFT theoretical framework where Kohn-Sham equation is formulated for a system with fixed number of electrons, external potential $V_{\mathrm{ext}}(\mathbf{r})$ can be also determined by the grand canonical ensemble of a given temperature and chemical potential.

A representative study along with this is Lozovoi's work in 2001.[5] The formalism of grand potential is suggested as

$$\begin{aligned}\Omega[\rho_e] &= -\frac{1}{\beta}\ln\det\left(1+e^{-\beta(H-\mu)}\right)\\ &\quad - \int d\bar{r}\rho_e(\bar{r})\left(\frac{V_H(\bar{r})}{2}+\frac{\delta\Omega_{xc}[\rho_e]}{\delta\rho_e(\bar{r})}\right)+\Omega_{xc}[\rho_e]\end{aligned} \tag{2.24}$$

where $\beta = \frac{1}{k_B T}$, V_H is Hartree potential and Ω_xc is exchange-correlation grand potential functional. The calculation of grand potential under $\mu = const.$ condition is possible with electron density gained by summing up the density over Kohn-Sham orbitals until the eigenvalues of the orbital reaches to the chemical potential μ. In order to avoid divergence in charged system with periodic boundary conditions, compensating excess background charge must be introduced to keep the system neutral. The properties of '$\mu = const.$' are restored by recalculating electrostatic potential with the correction caused by the compensating charge.

$$E_{\mathrm{es}} = \tilde{E}_{es} + \frac{q}{A_0}\langle\tilde{V}\rangle_{\Omega_0} + \frac{\pi q^2}{A_0^2}\left(\Lambda - \frac{L_z}{3}\right) \tag{2.25}$$

where $q,\ A_0,\ \Omega_0$ are the net charge, surface area of unit cell and volume of unit cell respectively, $\tilde{E}_{es}$ is electrostatic potential with background charge, Λ is z coordinate where potential is set to be zero as to behave as reference electrode, L_{z} is c-axis of the unit cell and $\langle\tilde{V}\rangle$ is average electrostatic potential. It should be noted that in contrast to $N_{\mathrm{e}} = const.$ mode, $\mu = const.$ mode compares the system with different charges. Thus, theoretical treatment of excess electron is much complicated than $N_{\mathrm{e}} = const.$ mode.

B. Micro canonical description; $N_e = const.$ model

In contrast to $\mu = const.$ model, most theoretical studies on electrode reaction have been based on $N_e = const.$ model. This approach can be classified into two whether it includes the effect of Helmholz layer or not; one is extrapolation scheme assuming computational hydrogen electrode which ignores the energetic contribution from Helmholtz layer at the interface. In this method, energetic contribution on redox reaction from electrode potential is varied by parameterized way. On the other hand, second method calculates required properties of a given atomic structure and determines the electrode potential by Fermi energy of the system. Second one is more sophisticated in that it enables to include the effect of Helmholtz layer, in other words, interaction between electric field and dipole at the interface is included. Electrode potential can be varied by introducing the artificial charges and compensating counter charges which makes additional dipole at the interface. A drawback of the second method is it requires the cancellation of undesired interaction relating to introduced counter charges as is similar to Lozovoi's study. However, theoretical treatment of second method is easier than '$\mu = const.$' and also easily applied to many systems. We will see the details of these methods in the followings.

B-1. Computational hydrogen electrode

An example of $N_e = const.$ model without Helmholtz layer is computational hydrogen electrode method proposed by Nørskov et al[6] for the purpose of estimating the electrocatalytic activity of oxygen reduction reaction on various metals. Energies of elementary steps on redox reaction including proton and electron can be handled in the following way (Figure 2-2):

1. The chemical potential of H^++e^- is equal to Gibbs free energy of $\frac{1}{2}H_2$ by setting standard hydrogen electrode (SHE) as the reference potential.

2. When electrode potential is varied, the total energy of each state is shifted by $-eU$ where e is the number of electrons in each redox step and U is electrode potential. This estimation is based on the approximation that the electrode potential only changes the energy of electrons.

The ignorance of Helmholtz layer is somewhat justified because an energetic contribution from Helmholtz layer is evaluated to be 0.015 eV under the condition of 1 V relative to the point of zero charge by assuming the width of the double layer to be ~ 3 Å. To calculate the Free energy of the elementary step, simple estimation of the energetic term contributed by zero point energy (ZPE) and entropy is also suggested. They simply added the ZPE of 0.07 eV for O adsorbed system and 0.3 eV for OH adsorbed system. This can be also justified because ZPE for O is mainly due to O vibration mode and OH is due to H vibration mode and variation of ZPE according to catalysts is smaller than the reaction energy scale. The entropic contribution is the sum of that in gas phase by estimating that from adsorbed species to be zero. This method enable us the systematic study for the research of new electrocatalysts and also detailed examination on the mechanical study. This method is applied to Chapter 3 and part of Chapter 4 in our study.

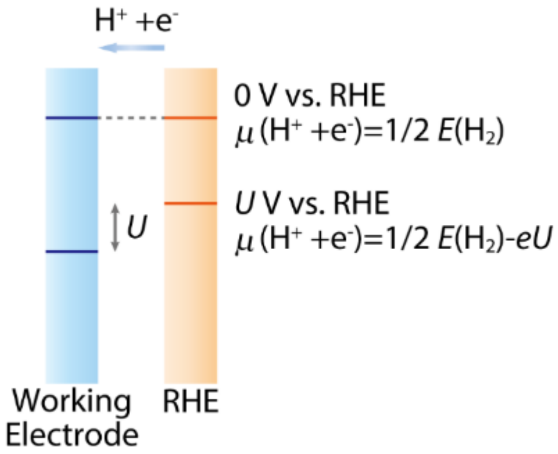

Figure 2-2. Schematic view of computational hydrogen electrode method

B-2. Electrode reaction with interfacial dipole

An improved way above the computational hydrogen electrode method is achieved by adding the contribution from interfacial dipole. The common feature is using the work function of the system to be a descriptor of electrode potential

$$U_{\mathrm{SHE}} = \frac{V(\infty) - E_{Fermi} - \Phi_{e^-}(\mathrm{SHE})}{e} = \frac{\Phi_{e^-} - \Phi_{e^-}(\mathrm{SHE})}{e} \qquad (2.26)$$

where Φ_{e^-} is a work function of the system and $\Phi(\mathrm{SHE})$ is standard hydrogen electrode potential relative to vacuum level, 4.44-4.8 eV. This approach requires the charge distribution which mimics the electrochemical system. Ways to introduce the charge distribution are various. The simplest one is adding a homogeneous background charge. A counter charge is expected to be distributed at electrode area making artificial capacitor system. A representative study is examined by Taylor in 2006.[7] They introduced homogeneous background charge and corrected the total energy due to undesired interaction. Unphysical distribution of added charge can be avoided by filling vacuum region with water molecules. They called this method 'double reference method'. Double reference method is possible within the framework of normal DFT. Another way of distributing charge is introducing neutral atoms having high or low electronegativity which is easily to be ionized. This can avoid artificial homogeneous background charge, however, undesired interaction of introduced atoms are not unavoidable. To vary the electrode potential in a fine grid, relatively large supercell is needed to make the relative charge distribution small. A representative study is done by Rossmeisl et al.[8] They varied the concentration of hydrogen to model various electrode potential. Here, we mention a double reference method which we will use in Chapter 4.

Double reference method

Double reference method is simulation technics for electrode/electrolyte system under applied potential. First, metal slab is charged up by $q = -n_e$ and compensating background charge $\rho_{bg} = -q/\Omega$ is introduced to prevent the divergence of electrostatic energy in periodic boundary condition. In order to avoid unphysical charge distribution, the aqueous region is filled with water of ambient density (system I, Figure 2-3(a)). The net charge distributed at interface makes water molecules polarizable and changes the position of Fermi level, i.e. electrode potential of given structures. To major the electrode potential at various net charge condition, two-step approach is employed; Fermi energy of two systems are set to be references.

Determination of electrode potential

A first reference is needed for the estimation of fermi energy relative to the vacuum level in system I. Similar to the way of determining work function in metal slab model, vacuum region is introduced to each side of system I large enough to converge the electrostatic potential at the boundary (system II, Figure 2-3(b)). The electrostatic potential in system II is shifted constantly so that the potential in vacuum region become zero (first reference),

$$\phi(z) = \phi'(z) - \phi'(v). \tag{2.27}$$

Here, $\phi(z)$ is the potential relative to vacuum level, ϕ'(z) and $\phi'(v)$ are the potential directly obtained by periodic boundary calculations at z position and vacuum region respectively. Assume that electrostatic potential in metal area relative to vacuum level is the same in system I and system II, we get

$$\phi_0(m) = \phi(m) = \phi'(m) - \phi'(v) \tag{2.28}$$

where m refers the metal region, ϕ with prime means the directly obtained results and underscored number (0 in 2.28) means the net charge in a system. Under this assumption, all the electrostatic potential in system I relative to vacuum level can be gained

$$\begin{aligned} \phi_0(z) &= \phi_0'(z) - \phi_0'(m) + \phi_0(m) \\ &= \phi_0'(z) - \phi_0'(m) + \phi'(m) - \phi'(v). \end{aligned} \tag{2.29}$$

Then fermi energy in system I relative to vacuum level can be determined via

$$\phi_0(f) = \phi_0'(f) - \phi_0'(m) + \phi'(m) - \phi'(v). \tag{2.30}$$

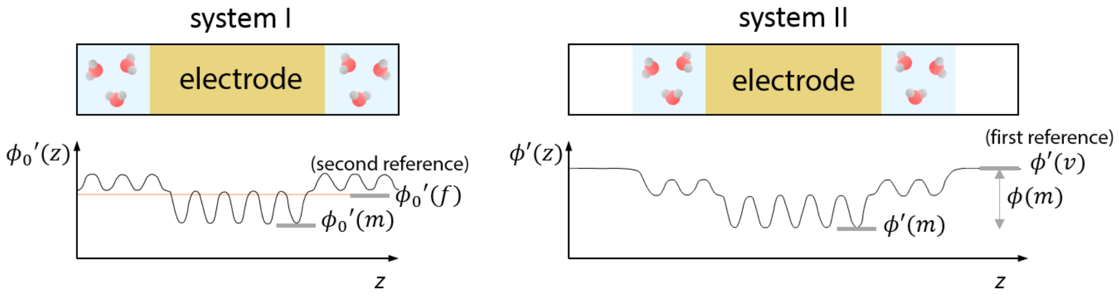

Figure 2-3. Schematic view of system I and system II and corresponding electrostatic potential

In charged system, electrostatic potential in vacuum region shows unphysical behavior, thus, the system is modeled by optimizing the geometry of the interface after adding the net charge to system I. During the optimization, aqueous region far from interface is kept fix to be reference point. The potential of position z or fermi energy of charged system relative to vacuum level is calculated via the potential at aqueous point in system I (second reference),

$$\phi_q(z) = \phi_q'(z) - \phi_q'(w) + \phi_0(w) \tag{2.31}$$

$$\phi_q(f) = \phi_q'(f) - \phi_q'(w) + \phi_0(w) \tag{2.32}$$

where ‘w’ refers position of aqueous region fixed during the optimization. Finally, electrode potential scaling to SHE at the given structure and net charge can be evaluated as

$$U_q = \frac{\Phi(\mathrm{SHE}) - \phi_q(f)}{e}. \tag{2.33}$$

Determination of the free energy

Although determination of free energy based on double reference method is not used in Chapter

4, I will note it because it is the center of the method. Ideally, chemical potential of the system must match the derivative of total energy with respect to q,

$$\mu = \frac{\partial \mathrm{E}}{\partial q} \quad . \tag{2.34}$$

Since background charge cause an unnecessary interaction, the total energy of charged system does not satisfy (2.34) and is not comparable without correction. Therefore, energetic contribution from background should be evaluated. The total energy of charged system is the sum of three terms;

$$E_{SCF} = E_{MW} + E_{MW/bg} + E_{bg} \tag{2.35}$$

where each term implies energy from metal/water interface, interaction between interface and background charge, and background charge respectively. The derivative of the energy is

$$\frac{\partial E_{SCF}}{\partial q} = \frac{\partial E_{MW}}{\partial q} + \frac{\partial E_{MW/bg}}{\partial q} + \frac{\partial E_{bg}}{\partial q}. \tag{2.36}$$

The second and third term is dependent on background charge that must be removed

$$\begin{aligned} \frac{\partial E_{MW/bg}}{\partial q} + \frac{\partial E_{bg}}{\partial q} &= \frac{\partial}{\partial q} \iiint \rho_{bg}(V_{MW} + V_{bg}) dxdydz \\ &= -\iiint \frac{V_{tot}}{\Omega} dxdydz. \end{aligned} \tag{2.37}$$

where V_{MW}, V_{bg} and V_{tot} are electrostatic potential arising from metal/water interface, background charge and both respectively.

Thus, we obtain

$$\frac{\partial E_{SCF}}{\partial q} = \mu - \iiint \frac{V_{tot}}{\Omega} dxdydz. \tag{2.38}$$

The corrected total energy of the system is then calculated as

$$E = E_{MW} = E_{SCF} + \int_0^q \left[\iiint \frac{V_{tot}}{\Omega} dxdydz \right] dQ. \tag{2.39}$$

The second term in (2.39) is approximated by the volume averaged electrostatic potential $\langle \bar{V}_{tot} \rangle$. In addition, correction term to account for the variation of charge will be added. Then, we get the final expression for free energy of the charged system

$$E = E_{SCF} + \int_0^q \langle \bar{V}_{tot} \rangle dQ + \mu q. \tag{2.40}$$

According to double reference method, they examined interfacial structure between water and Cu(111) and initial reaction step for the activation of methanol on Pt(111).

2.2.2 Description of pH in DFT

Due to an increased demand for disclosing pH dependent behavior in electrochemistry, an effect of pH should be addressed in DFT. Rossmeisl et al first address the effect of pH on electrochemical interfacial structure of Pt(111)/water.[9] I will review the method by following Rossmeisl's original paper. This method will be applied to RuO_2/water system in Chapter 5.

First, Born-Haber cycle for hydrogen oxidation is considered for the expression of chemical potential of protons and electrons, $\mu_{\mathrm{H^+ + e^-}}$.

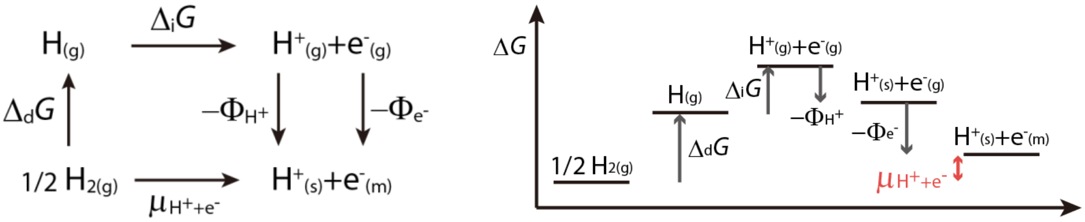

Figure 2-4. Born-Haber cycle for hydrogen oxidation

From Born-Haber cycle, $\mu_{\mathrm{H^+ + e^-}}$ can be written in terms of hydrogen dissociation energy in gas ($\Delta_{\mathrm{d}}G$), ionization energy of hydrogen atom in gas ($\Delta_{\mathrm{i}}G$), solvation energy of hydrogen ion ($\Phi_{\mathrm{H^+}}$), and work functions of electron in metal (Φ_{e^-}) respectively,

$$\mu_{\mathrm{H^+}+e^-} = \Delta_d G + \Delta_i G - \Phi_{\mathrm{H^+}} - \Phi_{e^-} \ . \tag{2.41}$$

Here, $\Delta_{\mathrm{d}}G$ and $\Delta_{\mathrm{i}}G$ are the energy relating to hydrogen gas/atom and not depending on the electrochemical system. Other two terms, $\Phi_{\mathrm{H^+}}, \Phi_{e^-}$, are variable associated with electrochemical environment. The pH dependence on $\mu_{\mathrm{H^+ + e^-}}$ arises from proton free energy in solution

$$\Phi_{\mathrm{H^+}} = \Phi^0_{\mathrm{H^+}} + 2.3k_B T \cdot \mathrm{pH} \ . \tag{2.42}$$

where $\Phi^0_{\mathrm{H^+}}$ refers solvation energy in standard condition. In standard hydrogen electrode condition (SHE) where $\mu_{\mathrm{H^+ + e^-}} = 0$ in pH = 0 ,

$$\mu_{\mathrm{H^+}+e^-} = \Delta_d G + \Delta_i G - \Phi^0_{\mathrm{H^+}} - \Phi_{e^-}(\mathrm{SHE}) = 0 \tag{2.43}$$

is satisfied. Thus the electrochemical potential $\mu_{\mathrm{H^+}+e^-}$ can be derived in terms of pH and work function as

$$\begin{aligned} \mu_{\mathrm{H^+}+e^-} &= \Phi_{e^-}(\mathrm{SHE}) - 2.3k_B T \cdot \mathrm{pH} - \Phi_{e^-} \\ &= -eU_{SHE} - 2.3k_B T \cdot \mathrm{pH} \, . \end{aligned} \tag{2.44}$$

Here, $\Phi_{e^-}(\mathrm{SHE})$ has been determined to be 4.44 eV - 4.8 eV in experiments and relationship between electrode potential and work function,

$$U_{SHE} = \frac{\Phi_{e^-} - \Phi_{e^-}(\mathrm{SHE})}{e} \qquad (2.45)$$

is used. In computational hydrogen electrode in B-1, electrochemical potential $\mu_{\mathrm{H}^+ + e^-}$ is just a parameter; it is varied without reference to the work function of a given structure (Figure 2-5(b)). The advantage of an evaluation by eq. (2.44) is that contributions from pH and electrode potential is consistent with a given water structures and associating dipole and electric fields at the interface (Figure 2-5(a)).

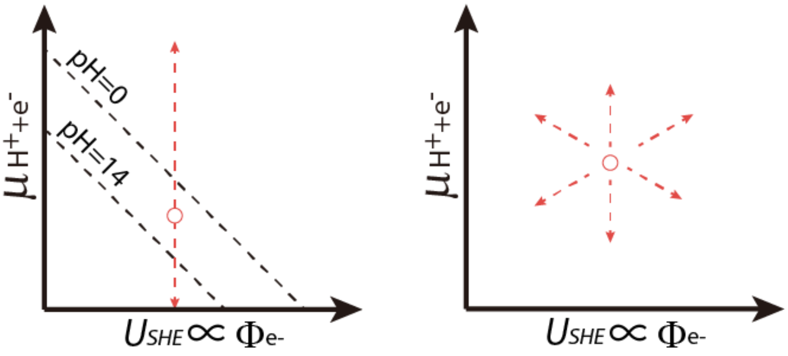

Figure 2-5. Comparative diagram of chemical potential represented in (a) eq. (2.44) and (b) computation al hydrogen electrode method

To disclose the interfacial structures, possible structures with variety of proton coverage and water orientation are surveyed and associated free energy values as functions of pH and electrode potential are calculated. Initially, the interfacial Gibbs free energy per surface atom was determined under the condition of reversible hydrogen potential (RHE), such that $\mu_{\mathrm{H}^{+}+e^{-}} = 0$, using the equation

$$G_{int}(\mu_{\mathrm{H}^{+}+e^{-}} = 0, \Phi_{e^{-}}) = \frac{\left\{G_{N,n} - G_{N,0} - \frac{n}{2} G_{\mathrm{H}_2}\right\}}{N} \tag{2.46}$$

where n and N represent the quantities of hydrogen and oxygen atoms, respectively, and $G_{N,n}$ is the Gibbs free energy of the structure having n hydrogen atoms on N surface oxygen atoms. The term $G_{int}\left(\mu_{\mathrm{H}^{+}+e^{-}}, \Phi_{e^{-}}\right)$ can then be introduced by varying $\mu_{\mathrm{H}^{+}+e^{-}}$ as follows:

$$G_{int}(\mu_{\mathrm{H}^{+}+e^{-}}, \Phi_{e^{-}}) = G_{int}(\mu_{\mathrm{H}^{+}+e^{-}} = 0, \Phi_{e^{-}}) - \frac{n}{N} \mu_{\mathrm{H}^{+}+e^{-}} \ . \tag{2.47}$$

Figure 2-6 shows three different ways of evaluating G_{int}. The pH dependent scheme here (Figure 2-6 (a)) is calculating G_{int} with the limitation of (2.44). It means G_{int} is projected onto pH plane including the effect of electrode potential and electric field. Figure 2-5 (b) is computational hydrogen electrode method where G_{int} dependence on $\mu_{\mathrm{H}^{+}+e^{-}}$ is linear. The work function dependence on G_{int} is not included in (b), which means an interaction between dipole and electric field is ignored. Figure 2-5 (c) shows the work function dependence on G_{int} meaning that only contribution from dipole electric field interaction is included. Calculating G_{int} on every possible interfacial structure with pH dependent scheme generally gives us the full information about G_{int}-U_{RHE} map projected onto pH-plane and structure with lowest G_{int} at every U_{RHE} is determined to be pH and electrode potential dependent interface.

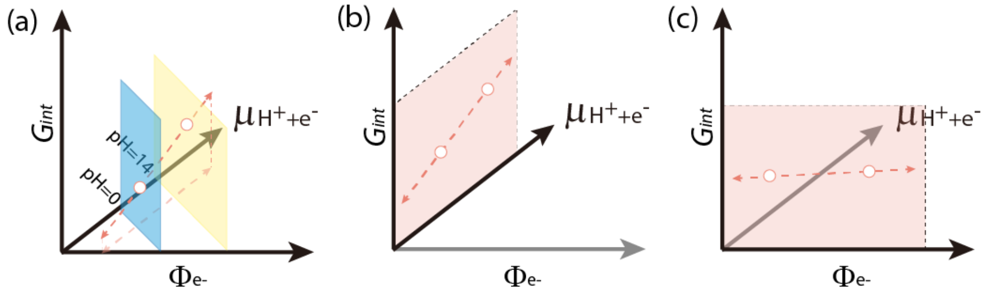

Figure 2-6. G_{int} plots as functions of $\mu_{\mathrm{H}^{+}+e^{-}}$ and $\Phi_{e^{-}}$. (a) G_{int} including effect of pH, electrode potential and electric field, (b) G_{int} including effect of electrode potential, (c) G_{int} including effect of electric field.

Reference

(1) R. M. Martin, Electronic Structure: Basic Theory and Practical Methods, 2008, Cambridge University Press

(2) S. Wilson, P. F. Bernath, R. McWeeny, Handbook of Molecular Physics and Quantum Chemistry, 2003, Wiley

(3) A. J. Bard, L. R. Faulkner, Electrochemical Methods: Fundamentals and Applications, 2000, Wiley

(4.) D. Mermin, *Phys. Rev.*, 1965, **137**. A1441

(5) A.Y. Lozovoi, A. Alavi, J. Kohanoff, and R. M. Lynden-Bell, *J. Chem. Phys.*, 2001, **115**. 1661

(6) J. K. Nørskov, J. Rossmeisl, A. Logadottir, L. Lindqvist, J. R. Kitchin, T. Bligaard, and H. Jónsson, *J. Phys. Chem. B*, 2004, **108**, 17886

(7) C. Taylor, S. Wasileski, J.-S. Filhol, and M. Neurock, *Phys. Rev. B*, 2006, **73**. 165402

(8) J. Rossmeisl, E. Skúlason, M. Björketun, V. Tripkovic, and J. Nørskov, *Chem. Phys. Lett.*, 2008, **466**.,68

(9) J. Rossmeisl, K. Chan, R. Ahmed, V. Tripković, and M. Björketun, *Phys. Chem. Chem. Phys.*, 2013, **15**, 10321–5.

Chapter 3

Electrocatalytic activity of oxygen reduction reaction on Ta_3N_5(100) surface

3.1 Introduction

The oxygen reduction reaction (ORR) and oxygen evolution reaction (OER) are the key reactions in both the cathode reaction of polymer electrolyte fuel cells (PEFCs) and the photo(electro)catalytic water-splitting reaction, respectively. In PEFCs, the ORR is the cathode reaction and the large overpotential of the ORR is the main cause for decreased efficiency[1]. Thus, to overcome the large overpotential, platinum catalysts are used. There have been numerous studies to clarify the mechanism for the ORR on Pt catalysts[2-5]. However, platinum is the precious metal that limits the widespread use of PEFCs; therefore, low-platinum or non-platinum catalysts for the ORR have been required, and various types of catalysts have been reported[6]. For example, as low platinum catalysts, alloy of Pt[7,8], core-shell structure with core of abundant metals[9], and Pt supported on nano-structuring carbon such as carbon nano-tubes[10] have been examined to reduce the amount of Pt used. As non-platinum catalysts, Fe and Co complex catalysts[11-14], carbon based catalysts[15-21], transition metal oxides, nitrides, and oxynitride catalysts[22-35], such as Ta_3N_5, TaNO, TaCNO, ZrO_xN_y, and NbO_xN_y, have been reported. Among all, transition metal oxide, nitride and oxynitride catalysts have an advantage of being stable in an acid environment[28,30] and are the promising materials for ORR non-platinum catalysts.

In the case of the photo(electro)catalytic water-splitting reaction, transition metal nitrides and oxinitrides have attracted much interest as well for the promotion of the water-splitting reaction under visible light conditions[36]. Among them, Ta_3N_5 is one of the most promising materials because of the band gap of 2.1 eV suitable for the visible light absorption and its conduction band (CB) and valence band (VB) position straddling the H^+/H_2 and O_2/H_2O redox potential[37-39]. Therefore, research on Ta_3N_5 has focused on its optical properties and there have been fewer reports on the surface reactions of Ta_3N_5. However, OER is the reverse reaction of ORR, so that if the reaction site for ORR on Ta_3N_5 surface is effective, the OER in photocatalytic water-splitting can be promoted on the same site. Therefore, control of the ORR is the major issue to achieve a hydrogen energy system and the investigation of the ORR on Ta_3N_5 is useful for the improvement of both fuel cells and water-splitting systems.

In this Chapter, our focus is on improving the ORR activity on Ta_3N_5 by clarifying the reaction mechanism for oxygen reduction. Surface reactions on Ta_3N_5 have been reported partially, such as oxygen adsorption[40] and water adsorption[41], however, a fully calculated energy diagram of the ORR have not been reported. It is reported by XPS experiments that surface of Ta_3N_5 is so oxidized that the ratio of surface oxygen atom and nitrogen atom is almost 1:1 after synthesis[28]. It is also reported that such O-substitution to surface N atoms is thermodynamically stable in both bulk and surface region from DFT calculations[40,42]. Therefore we analysed the mechanism of oxygen reduction reaction on clean and O-substituted Ta_3N_5. We also discuss how to improve the ORR activity on Ta_3N_5 surface.

3.2 Method

DFT calculations were performed using the SIESTA code[43]. The exchange correlation energy was calculated with a generalized gradient approximation (GGA) using the RPBE functional[44]. A double-z split-valence basis set with polarization orbitals for all elements[45] and norm-conserving pseudopotentials proposed by Troullier and Martins[46] were used. Spin polarized calculations were performed on all the system in our calculations. Geometry optimization was performed until the maximum atomic force was smaller than 0.02 eV/Å. The transition state was calculated using the nudged elastic band (NEB) method[47-49]. The energies were sampled on (1×2×2) grid with the Monkhorst-Pack method[50] which shows the total energy convergence within 1 meV/atom.

3.3 Results and discussion

3.3.1 Modeling Ta_3N_5 clean surface

Ta_3N_5 is known to have pseudobrookite structure. It has orthohomobic/Cmcm group including 32 atoms in conventional unit cell[51]. The optimized size of the Ta_3N_5 unit cell was *a*=3.99 Å, *b*=10.69 Å, *c*=10.69 Å, where each lattice parameter almost matches the experimental data[51] (*a*=3.88 Å, *b*=10.21 Å, *c*=10.26 Å). First, we carried out the model calculations to determine the size of the slab by analyzing the effects of the surface state. We started with (100) surface because Ta_3N_5 is layered structure to [100] direction and is easy to make various size of the slab models. We constructed 4-layer slab model as minimum size and 14-layer slab model as maximum size. We added 20 Å thick of vacuum space between slabs and optimized the structure with fixing the center 32 atoms i.e. center 2 layers. To analyze the effects of the surface state on each slab model, band gap and surface energy are evaluated. The surface energy is defined as the energy difference between slab and bulk models per area defined as follows,

$$E_{\mathrm{surf}}=\{E(\mathrm{slab})-nE(\mathrm{bulk})\}/2A \tag{3.1}$$

where E(slab) and E(bulk) represent total energy of the slab and bulk models respectively, n is the number of unit cells used to make slab model (n=2~7 in this case), and A represents the surface area. The band gaps and surface energies as a function of the slab model size are shown in Figure 3-1(a) and (b). Both band gaps and surface energies converged from 8-layers. The slab model of 8-layers consists of center fixed 2-layers and two surface 3-layers in each side. This indicates that the slab models including at least three relaxed layers are good models to represent Ta_3N_5 surface. Therefore, 6-layer model including at least three relaxed layers are employed as surface models for the calculation of oxygen adsorptions and oxygen reduction reactions.

The stabilities of other surfaces such as (010) and (001) are also evaluated. The (010) and (001) surfaces are not layered structures and we cannot clearly define the number of layers. Therefore, we first construct the triple-sized cell which have a cube-like structure (a=11.97 Å, b=10.69 Å, c=10.69 Å) including 6-[100] layers and then pile two triple-sized cell to [010] direction to make (010) surface and [001] direction to make (001) surface with 20 Å vacuum space. Size of the calculated model of (100) surface is equivalent to the 12-layer (100) surface model. Since all three models include 192 atoms with fixed center 32 atoms, we consider that the size of the (010) and (001) surface models is enough. Calculated surface energies of (100), (010),

(001) surfaces are 0.067 eV Å^{-2}, 0.072 eV Å^{-2}, and 0.081 eV Å^{-2}, respectively. Since the surface with the lowest surface energy is the most stable by definition, the (010) and (001) surfaces are considered to be unstable. The atomic arrays in the (010) and (001) surfaces are unlevel, while the (100) surface is stoichiometric and has plane atomic arrays which contribute to the low surface energy. Other surfaces such as (111) are not likely to be more stable than (100) surface from the same reason. Through these calculations, the (100) surface is assumed to be exposed in wide area. Furthermore, electrochemical environment for oxygen reduction reaction is highly oxidative condition that surfaces with higher surface energies are not likely to be stable. Therefore we study the oxygen reduction reaction on Ta_3N_5 (100) surface. The oxygen reduction reaction were examined using one reaction site per 6-layer model which corresponds to the coverage of 0.88 molecule/nm^{-2}. Although there is no direct comparable experimental data, the O_2 temperature-programmed desorption (TPD) on TiN and Pt show the O_2 adsorption density of 0.18-0.57 molecule nm^{-2} on TiN and 2.1 molecule/nm^{-2} on Pt.[24] Thus, the difference of our calculation model and the experimental adsorption density is considered to be small. To make the O-substituted surfaces, one (O1-substituted surface) or two (O2-substituted surface) of the surface nitrogen atoms are replaced by oxygen atoms. The structures of clean, O1-substituted and O2-substituted surfaces are shown in Figure 3-2(a)-(c). On the clean surface, Ta sites in the unit cell are labelled from A to F, as shown in Figure 3-2(d). Sites A, C, D and F are geometrically equivalent, as are sites B and E.

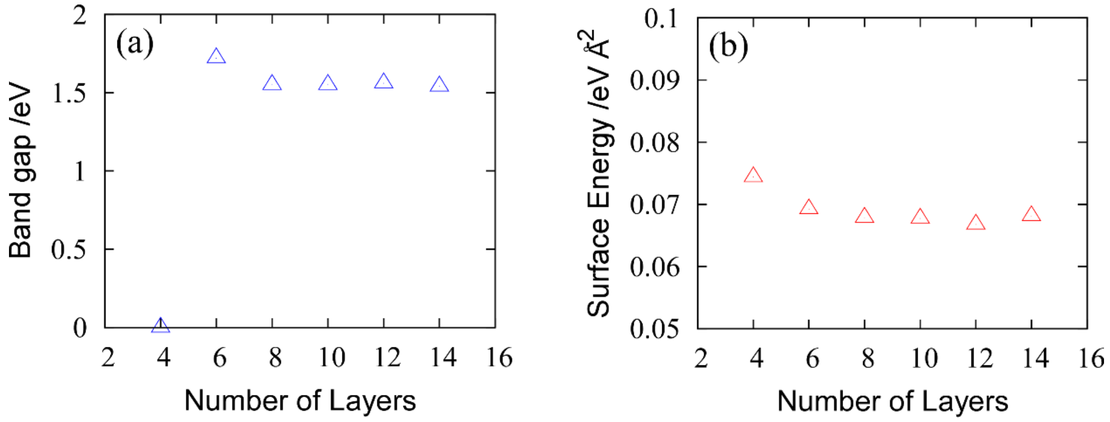

Figure 3-1. (a) Calculated bandgap energy (*U*=5.0 eV) as a function of the number of layers. Bandgap energy converged to about 1.5 eV at 8-layers. (b) Calculated Surface energy as a function of the number of layers. Surface energy converged to about 0.067 eV Å^{-2} at 8-layers.

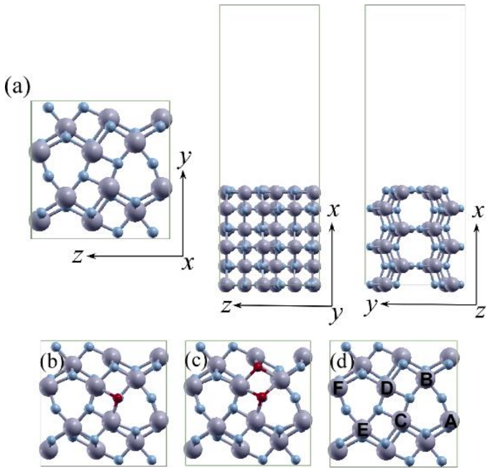

Figure 3-2. The Ta_3N_5 (100) structures of (a) clean surface from *x*, *y* and *z* directions (b) O1-substituted surface from *x* direction, (c) O2-substituted surface from *x* direction and (d) labeling of surface six Ta atoms in unit cell from *x* direction. The big purple atoms are Ta, small blue atoms are N and small red atoms are O.

3.3.2 Surface structures and oxygen adsorption structures

As the first elementary step of the ORR, oxygen adsorption on clean and O-substituted surfaces was examined, assuming molecular adsorption. The structures of molecular adsorption are classified into three types: Pauling-type (end-on adsorption), Griffiths-type (side-on adsorption on one surface atom), and Yeager-type (side-on bridge adsorption between two surface atoms). The examples of three type's oxygen adsorption structures on O2-substituted surface were pictured in Figure 3-3. Considering the symmetry, the energies for Pauling-type and Griffiths-type adsorption were calculated only for sites A and B for a clean surface, while the energies of Yeager-type adsorption were calculated between the A-B, A-C and C-D sites. On O-substituted surfaces, the symmetry was broken due to the O-substitution and the adsorption energies for the three-types of structures were calculated for every possible site. We assumed that strong oxygen adsorption sites can be active sites for the ORR.

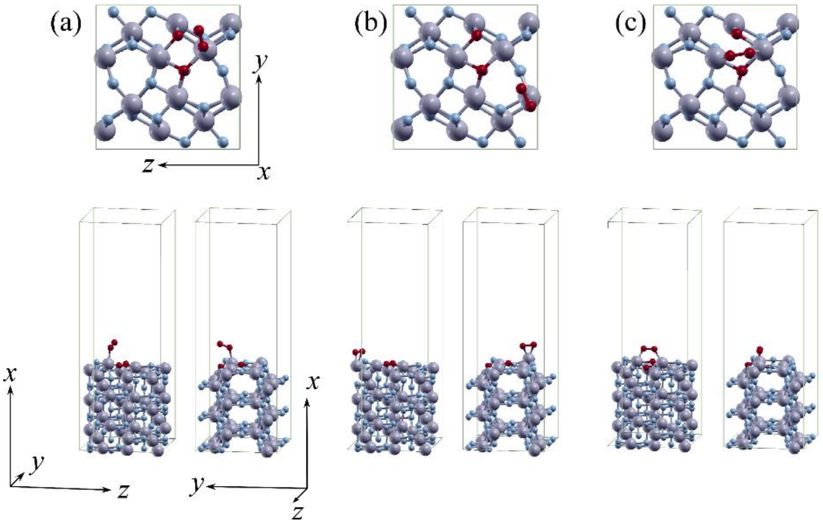

Figure 3-3. The structures of oxygen molecular adsorption of (a) Pauling-style at B site, (b) Griffiths-style at A site, and (c) Yeager-style between B and D on O2-substituted surface from three directions. The big purple atoms are Ta, small blue atoms are N and small red atoms are O.

The adsorption energy of oxygen molecule is defined as

$$E_{ad} = E(surf + \mathrm{O}_2) - \{E(surf) + E(\mathrm{O}_2)\} \tag{3.1}$$

where $E(surf + \mathrm{O}_2)$, $E(surf)$ and $E(\mathrm{O}_2)$ are the respective energies of the surface with adsorbed O_2, only the surface, and O_2 itself. The negative value of E_{ad} means that the adsorption of oxygen on the surface is exothermic. The theoretically obtained adsorption energies for Pauling-type and Griffiths-type adsorption on clean and O-substituted surfaces are shown in Table 3-1(a). The adsorption energies for Yeager-type adsorption were also calculated and are listed in Table 3-1(b).

The adsorption energies on the clean surface range from 0.05 to -0.06 eV in Table 3-1. Therefore, the oxygen molecules cannot adsorb at any sites on the clean surface. However, oxygen molecules can adsorb strongly on both the O1-substituted and O2-substituted surfaces because all E_{ad} in Table 3-1 are negative. Here we investigated the relationship between the adsorption energies and the number of substituted oxygen atoms for Pauling-type, Griffiths-type and Yeager-type adsorption. A comparison of the energy distribution on clean, O1-substituted and O2-substituted surfaces indicated that oxygen molecules strongly adsorb when the number of surface substituted oxygen atoms increases.

Next, the adsorption energies of each adsorption type were compared. The results of both O1-substitued and O2-substituted surfaces show that oxygen molecules with the Griffiths-type structure adsorb stronger than those with the Pauling-type structure. This is because one Ta-O bond is formed in Pauling-type adsorption, whereas two Ta-O bonds are formed in Griffiths-type adsorption. The activation energy of the structural change from Pauling-type adsorption to Griffiths-type adsorption on B and C sites was examined on O1-substituted and O2-substituted surfaces. The calculated activation energy is as large as 0.3 eV. The adsorption energies of Pauling-type structures are weaker than those of Griffiths-type structures and the activation energies from Pauling-type to Griffiths-type adsorption is not so high; therefore, we consider that all Pauling-type adsorption changes to Griffiths-type adsorption on every site. In the case of Yeager-type adsorption, oxygen molecules can adsorb on every site on O1-substituted and O2-substituted surfaces. Figure 3-4 shows the relationship between the adsorption energy and Ta-Ta bond length. From the analysis, oxygen molecules were determined to strongly adsorb between closely located Ta atoms. The same trend can be seen on O1-substituted surface as well (see Table 3-1(b)). From analysis of oxygen adsorption on O-substituted surfaces, two types of adsorption sites were determined to be possible active sites. One is Yeager-type adsorption between two closely located Ta atoms, and the other is Griffiths-type adsorption on every Ta atom in the O-substitution structure. Therefore, we consider that the ORR starts from these two types of O_2 adsorption.

From experiments, O_2 adsorption was reported by TPD. The estimated O_2 adsorption energy on Ta_3N_5 nanoparticle is about 0.3 eV (desorption peak around 110 – 120 K). By taking into account the entropic contribution to the free energy at 110-120 K (S=205.138 J K^{-1} mol^{-1} from the database[52]), 0.5-0.6 eV of the adsorption energy in our results are reasonable. This value is between that on clean surface and O1-substituted surface. It should be noted that considering the lack of van der Waals interactions in our calculations and the impurities left on Ta_3N_5 nanoparticle in real system, it is difficult to compare the adsorption energy directly. However, investigation of the surface reaction on model system is in general the basis for the design of catalysts. Thus, we focused on the discussion comparing clean surface and O-substituted surface using the model system.

Table 3-1. (a)Calculated adsorption energy for Pauling-type or Griffiths-type O_2 adsorptions. The 'site' column shows the positions of O_2 adsorption shown in Figure 3-2(d). In middle column, 'style', shows adsorption type, G means Griffiths-type structure and P means Pauling-type structure. (b)Calculated adsorption energy for Yeager-type structure together with the adsorbed Ta-Ta length in the middle column.

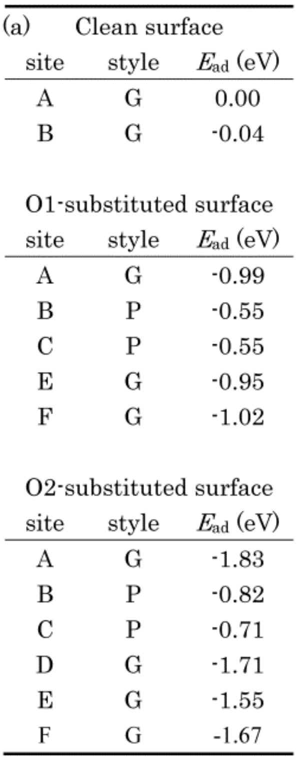

(a) Clean surface

site	style	E_{ad} (eV)
A	G	0.00
B	G	-0.04

O1-substituted surface

site	style	E_{ad} (eV)
A	G	-0.99
B	P	-0.55
C	P	-0.55
E	G	-0.95
F	G	-1.02

O2-substituted surface

site	style	E_{ad} (eV)
A	G	-1.83
B	P	-0.82
C	P	-0.71
D	G	-1.71
E	G	-1.55
F	G	-1.67

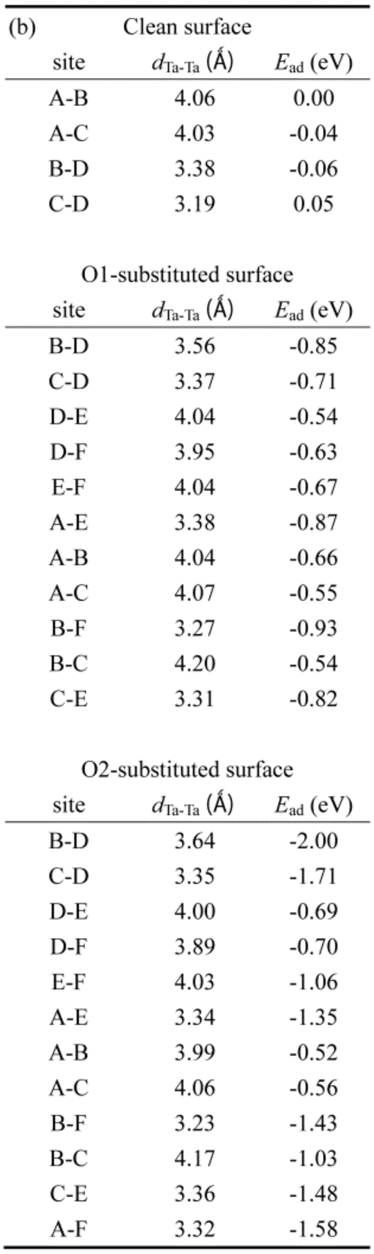

(b) Clean surface

site	$d_{Ta\text{-}Ta}$ (Å)	E_{ad} (eV)
A-B	4.06	0.00
A-C	4.03	-0.04
B-D	3.38	-0.06
C-D	3.19	0.05

O1-substituted surface

site	$d_{Ta\text{-}Ta}$ (Å)	E_{ad} (eV)
B-D	3.56	-0.85
C-D	3.37	-0.71
D-E	4.04	-0.54
D-F	3.95	-0.63
E-F	4.04	-0.67
A-E	3.38	-0.87
A-B	4.04	-0.66
A-C	4.07	-0.55
B-F	3.27	-0.93
B-C	4.20	-0.54
C-E	3.31	-0.82

O2-substituted surface

site	$d_{Ta\text{-}Ta}$ (Å)	E_{ad} (eV)
B-D	3.64	-2.00
C-D	3.35	-1.71
D-E	4.00	-0.69
D-F	3.89	-0.70
E-F	4.03	-1.06
A-E	3.34	-1.35
A-B	3.99	-0.52
A-C	4.06	-0.56
B-F	3.23	-1.43
B-C	4.17	-1.03
C-E	3.36	-1.48
A-F	3.32	-1.58

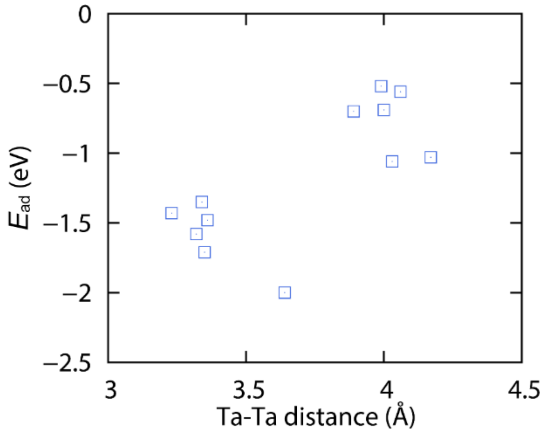

Figure 3-4. Adsorption energies of Yeager-type structure on O2-substituted surface are shown as a function of the distance between adsorption sites of two Ta atoms.

3.3.3 Mechanism for the ORR on clean and O-substituted surfaces

In this section, we examine the mechanism for the ORR starting from Yeager-type and Griffiths-type adsorption on clean and O-substituted surfaces. As an example of an O-substituted surface, the O2-substituted surface (Fig. 3-2(c)) was selected because the effect of O-substitution is stronger on the O2-substituted surface than that on the O1-substituted surface. The active sites for the oxygen reduction reaction were determined to be B-D site in Yeager-type adsorption and A site in Griffiths-type adsorption because the adsorption energy on these two sites are strongest among other sites (see Table 3-1, the data about O2-substituted surface).

Both 4-electron and 2-electron reactions on clean and O2-substituted surfaces were considered as mechanisms for the ORR. The 4-electron and 2-electron reactions are:

$$O_2 + 4H^+ + 4e^- \rightarrow 2H_2O \quad \text{(4-electron)}$$

$$O_2 + 2H^+ + 2e^- \rightarrow H_2O_2. \quad \text{(2-electron)}$$

It has remained controversial which reaction occurs, even on a Pt surface, although the 4-electron reaction is considered to be favourable. Therefore, we examined the possibilities of both reactions on clean and O2-substituted Ta_3N_5 surfaces. The reaction difference between 4-electron and 2-electron reaction is whether O-O bond breaking occurs or not. We assumed that O-O bond breaking is likely to occur when oxygen molecule adsorbs between two Ta sites. By contraries, oxygen reduction without O-O bond breaking is likely to proceed when oxygen adsorb on one Ta sites. Based on this assumption, the energy diagram of 4-electron reaction from Yeager-type oxygen adsorption and 2-electron reaction from Griffiths-type oxygen adsorption were calculated. The energy diagrams of 4-electron and 2-electron reactions on clean and O2-substituted surfaces were examined by the frequently used method for the electrochemical reaction originally suggested by Nørskov et al[2]. Here, we treat the energy of ($H^+ + e^-$) to be equal to that of $\frac{1}{2}H_2$ to take into account the reaction under the condition of 0.0 V vs. SHE (standard hydrogen electrode). The entropic effect and zero-point energy (ZPE) correction were included for the calculation of H_2 and O_2 molecules using the database[52]. For the adsorbed species, the entropic effect can be ignored and the only ZPE correction of 0.07 eV for O* and 0.3 eV for OH* was added following to ref. 2. For a water-adsorbed system, ZPE is estimated to be 0.6 eV, which is twice that of an OH-adsorbed system. ZPE corrections in our system can be justified because they are originated to the O-H vibration and not heavily depending on the kinds of the surfaces. For example, ZPE corrections were calculated on TiO_2 (110) to be 0.05 eV for O*, 0.35 eV for OH* and 0.7 eV for OH_2*[53]. On α-Fe_2O_3 system, they are 0.04 eV for O*, 0.37 eV for OH* and 0.67 eV for OH_2*[54]. The difference among the system is within 0.1 eV. The adsorption energies of intermediates were calculated using this method with basis set superposition error (BSSE) and dipole corrections. To consider the water affinity effect, three water molecules were added for the surface including OH* and H_2O* species. Here we use "*" to denote an adsorbed species.

A. Reaction mechanism starting from Yeager-type adsorption

The mechanism for the ORR on a clean surface starting from Yeager-type oxygen adsorption for the 4-electron reaction was examined first. The calculated energy diagram and the structures of the adsorbed species at each step are shown in Figures 3-5 and 3-6, respectively. Because O_2 itself cannot adsorb onto the clean surface, oxygen first adsorbs together with (H^++e^-) and then forms OOH* (step 2). The adsorbed O-O bond is broken with the second (H^++e^-) transfer to form O* and H_2O* (step 3) without an energy barrier. H_2O then desorbs from the surface and the O* species (step 4) remains. Following the subsequent (H^++e^-) transfer, H_2O* is formed again (step 6). The second H_2O desorption is the rate-determining step that requires an energy of 1.28 eV (step 7). During the geometry optimizations, the reaction path forming 2OH* after the second (H^++e^-) transfer cannot be found in our calculations. The second H_2O desorption energy is higher compared to the first H_2O desorption energy. Zou et al investigated the water adsorption and dissociation on Ta_3N_5 (100) surface by DFT calculations[41]. They claimed the dangling bond strongly adsorb water on surface. Similar to this mechanism, in the present study, the clean surface with adsorbed O* is positively charged (Mulliken charge of adsorbed O* is -0.40), which means the reduction of dangling bond on the surface. This leads to the decrease of the first H_2O desorption energy. From our calculations, the bottleneck for the reaction is water desorption at the last step. It should be stressed that O_2 cannot adsorb without (H^++e^-) on the clean surface; therefore, almost all the active sites may be covered by other molecular species such as H_2O* and OH*. The adsorption of these species can also decrease the catalytic activity.

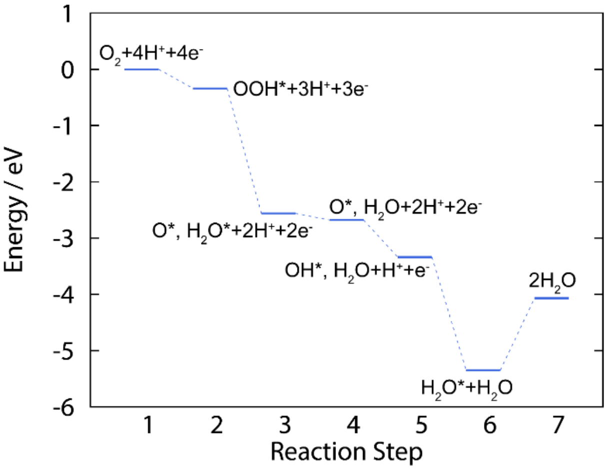

Figure 3-5. Calculated energy diagram of ORR on clean surface. The formation energy of H_2O at step 7 is calculated in the gas phase model to be 4.07 eV

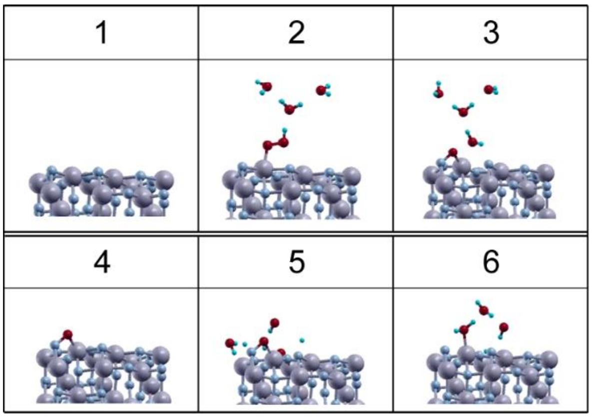

Figure 3-6. Structures of adsorbed species at each reaction step of ORR. The number corresponds to the number of reaction step in Fig. 3-4.

Next, the mechanism for the ORR on an O2-substituted surface starting from Yeager-type oxygen adsorption for the 4-electoron reaction was examined. The calculated energy diagram and structures of the adsorbed species are shown in Figures 3-7 and 3-8, respectively. An oxygen molecule first adsorbs strongly on the O2-substituted surface. The O-O bond then breaks when (H^++e^-) transfers to form O* and OH* (step 3) without any energy barrier. After consecutive (H^++e^-) transfer, O* and H_2O* is produced (step 4). Energy of 0.82 eV is required for the first water desorption (from step 4 to step 5). The second water desorption (from step 6 to step 8) requires the energy of 0.94 eV. From our calculations, the rate determining step for the reaction on an O2-substituted surface is also the water desorption. The energy barrier for the water desorption is less than that for a clean surface. Therefore, the O2-substituted surface has higher ORR activity. However, the stable OH* and H_2O* species decrease the catalytic activity, as shown by the dashed line in Figure 3-7 (step 4 and step 5).

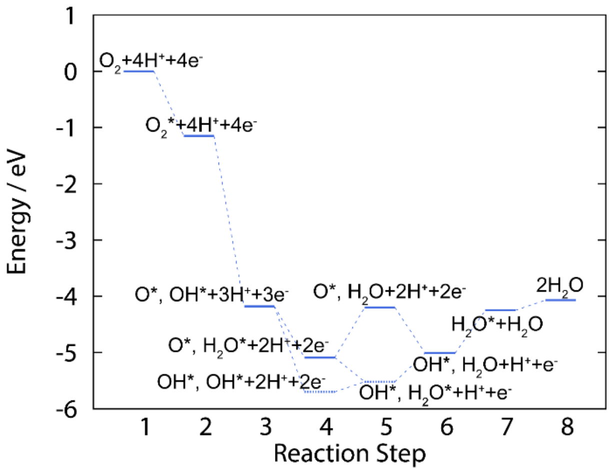

Figure 3-7. Calculated energy diagram of ORR on O2-substituted surface.

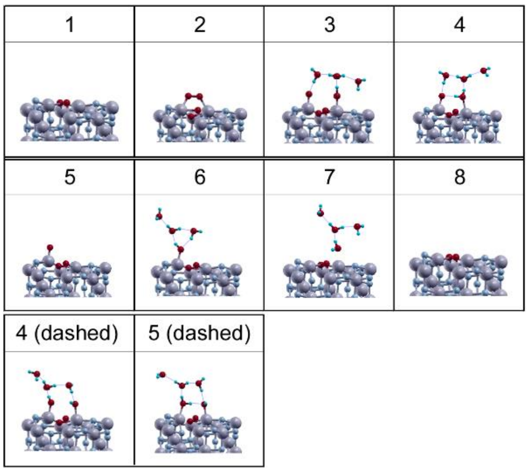

Figure 3-8. Structures of adsorbed species at each reaction step of ORR. The number corresponds to the number of reaction step in Fig. 3-7.

B. Reaction mechanism starting from Griffiths-type adsorptions

An energy diagram was next calculated for the ORR which starts from Griffiths-type adsorption for the 2-electron reaction. The calculated energy diagram is shown in Figure 3-9 together with the structures of adsorbed species on the O2-substituted surface. The red and blue lines represent the energy for the ORR on clean and O2-substituted surfaces, respectively. On the clean surface, oxygen adsorbs onto the surface with (H^++e^-) (step 3) and the reaction proceeds to generate H_2O_2* (step 4). The H_2O_2 desorption energy is approximately 0.84 eV (step 5). On the O2-substituted surface, oxygen adsorbs strongly onto the surface (step 2) and OOH* is generated (step 3). An energy of 0.81 eV is required from OOH* to produce desorbed H_2O_2 (step 4). Our calculations indicate that the 2-electron reaction proceeds on the O2-substituted surface rather than on the clean surface because of the stronger O_2 adsorption energy and slightly smaller H_2O_2 desorption energy on O2-substituted surface. Compared with experimental data, the H_2O_2 formation energy of 0.59 eV is relatively smaller than that in the database[52] (1.25 eV) because the energy is calculated in a gas phase model in the present study. Therefore, we inserted experimental data for step 5 to elucidate that H_2O_2 production proceeds with the little energy barrier. It should be noted that production of H_2O by the decomposition of H_2O_2 requires the same energy as to produce H_2O from O_2 molecule because part of reaction coordinate is common in which rate-determining step is involved. By comparing the 4-electron and 2-electron reactions, the smaller energy barrier on the 2-electron reaction shows that the main product on the Ta_3N_5(100) surface is H_2O_2, which is in good agreement with the experimental report that suggests hydrogen peroxide is obtained on metal oxide and nitride catalysts.[24]

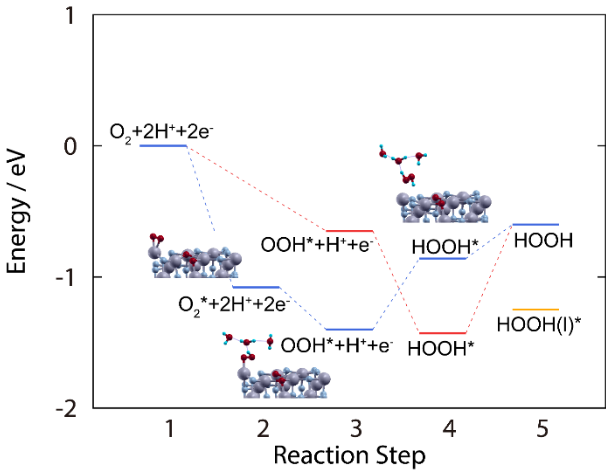

Figure 3-9. Calculated energy diagram of H_2O_2 production on clean and O2-substituted surface. The red line shows the reaction on clean surface and blue line shows the reaction on O2-substituted surface. Corresponding structures are shown as the snapshot of each reaction step on O2-substituted surface. The yellow line at step 5 is derived experimental formation energy of $H_2O_2(l)$[54].

3.3.4 Difference in catalytic activity between clean and O-substituted surfaces

A comparison of the reaction on clean and O2-substituted surfaces indicates that the O2-substituted surface has higher catalytic activity than the clean surface. The small adsorption energy of O_2 may be the bottleneck for the 4-electron and 2-electron reactions on a clean surface. OH and H_2O adsorb strongly onto the clean surface; therefore, the surface sites are covered by water, which suppresses O_2 adsorption. On the other hand, O_2 adsorbs strongly onto the O2-substituted surface and the probability of starting the reaction is higher than on the clean surface. In addition, the H_2O and H_2O_2 desorption energy is smaller than on the clean surface. A summary of the energy diagram calculations indicates that the O2-substituted surface has higher catalytic activity because of strong O_2 adsorption energy and smaller H_2O_2 desorption energy. It should be noted that O2-substituted surface is one model system for the oxidized surface. Considering O_2 adsorption energy reported by experiment is between that on clean surface and O1-substituted surface, oxygen reduction reaction possibly occurs at partially oxidized Ta_3N_5 surface.

3.3.5 Origin of catalytic activity on Ta_3N_5(100) surface

From the discussions in sections 3.3.3 and 3.3.4, the difference of the catalytic activity for the ORR on clean and O2-substituted surfaces is determined to be the O_2 adsorption energy and H_2O/H_2O_2 desorption energy. Our previous calculations of the density of states (DOS) for clean and O-substituted surfaces show that an impurity state appears between the CB and VB on the O-substituted surface, which allows O_2 adsorption[40]. The impurity state can attack O_2 π^* anti-bonding orbitals to weaken the O-O bonds, which leads to O_2 chemisorption on the surface. The ORR catalytic activity is significantly related to the O_2 adsorption energy; therefore, the impurity state is essential for the catalytic activity of non-conductive transition metal oxides or nitrides. In particular, when the π* orbital of O_2 is located above the VB in a semiconductor, the transfer of electrons from the semiconductor surface to O_2 molecule is difficult without the impurity state. In this context, the adsorption (binding) energies of O_2 and OH on clean and O-substituted surfaces were examined, and the calculated energies are given in Table 3-2. The O_2 adsorption energy changed significantly from 0.0 eV (on the clean surface) to -2.0 eV (on the O2-substituted surface), and the adsorption energy of OH changed from -2.3 eV (on the clean surface) to -3.3 eV (on the O2-substituted surface). Thus, OH interacts strongly even on the clean surface. The variety of O_2 adsorption energies contributes to the difference in catalytic activity between the clean and O-substituted surfaces and the strong binding energy of OH leads to the endothermic water desorption energy even on the O2-substituted surface. Finally, effect of Hubbard U parameter on the binding energy was investigated. The parameter (U=5.0 eV) was selected to recover the experimental band gap (2.1 eV[39]) in the bulk system. The calculated O_2 adsorption energies were -0.71 eV and -1.21 eV, and OH binding energies were -2.7 eV and -2.9 eV on O1-substituted and O2-substituted surfaces respectively. All the values are reduced and Hubbard U correction affects the energy diagram. The decrease rate of the O_2 adsorption energies are 21 % and 40 % and the decrease rate of the OH binding energies are 21 % and 40 % on O1-substituted and O2-substituted surfaces respectively. Because the adsorption of O_2 needs the electron donation from the surface, it strongly depends on the level of the impurity states easily affected by the Hubbard U correction. On contrary, OH binding energy dependence on the correction is relatively small. Thus, the energy from OH* (step 6 in Figure 3-7) to produce water (step 8 in Figure 3-7) on O2-substituted surface may not be largely affected by Hubbard U corrections.

3.3.6 Strategy to control ORR activity

From discussions in the last subsections, a strategy for the higher ORR activity can be achieved by controlling the energy level of the impurity state. Therefore, the energy levels of the O2-substituted Ta_3N_5 surface and reactant molecules (O_2, OH) were analysed by calculation of the DOS. The relative energies of O_2 and OH to the O2-substituted surface are calculated by setting the same vacuum level. The DOS calculated for Ta_3N_5, O_2 and OH are shown in Figure 3-10(a). The distribution of the impurity state for Ta_3N_5 (red line) crosses the Fermi energy. The singly occupied molecular orbital (SOMO) of O_2 (blue line) has an energy peak at -2.3 eV and the SOMO of OH (yellow line) has an energy peak at -1.2 eV. By considering the interaction with the Ta impurity state, the energy peak for the SOMO of OH is closer than that for O_2 (see Figure 3-10(b)). This means that interaction between the impurity state and SOMO of OH is strong, which leads to the stable adsorption of OH*. Therefore, the O_2 and OH adsorption energies can be controlled by changing the energy level of the impurity state.

Let us consider how to improve the ORR activity. To enable O_2 adsorption on the surface, the impurity state must be located above the SOMO level of O_2. In contrast, to decrease the OH binding energy, the impurity state is better located far away from the SOMO level of OH. Therefore, the target energy for the impurity state is above the SOMO level of O_2 and under the SOMO level of OH. Thus, to improve the ORR activity, we propose the (co)doping of carbon atoms in accordance with oxygen. O-substitution on nitrides donates electron that makes the impurity state below the CB that can act as d band in metal catalysts. On contrary, C-substitution donates hole that undershifts the energy level of the impurity state. Thus, C-substitution could possibly weaken the binding energy of OH while keeping the energy of the impurity state above the SOMO level of O_2. This is consistent with experimental results for the order of catalytic activity among Ta_3N_5, TaON and TaCNO[23,32], where TaCNO has the highest activity; TaCNO>TaON>Ta_3N_5.

Table 3-2. Calculated adsorption energy of O_2 and OH with Ta_3N_5 (100) surfaces.

	O_2*	OH*
Clean surface	-0.1 eV	-2.3 eV
O1-substituted surface	-0.9 eV	-3.0 eV
O2-substituted surface	-2.0 eV	-3.3 eV

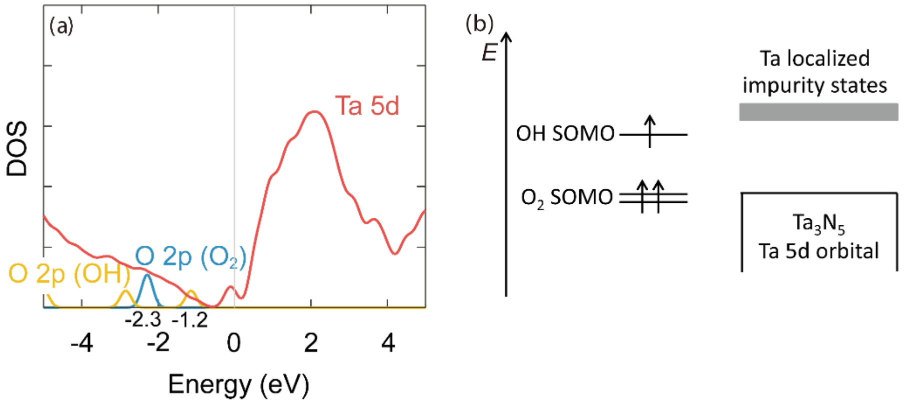

Figure 3-10 (a) Calculated DOS of Ta_3N_5 O2-substituted surface, isolated O_2 and OH are shown. The red line shows the contribution of Ta 5d orbital in Ta_3N_5, blue line shows the contribution of O 2p orbital in O_2, the yellow line shows the contribution of O 2p orbital in OH respectively. The energy peak of -2.3 eV in blue line corresponds to O_2 SOMO orbital and the energy peak of -1.2 eV in yellow line corresponds to OH SOMO orbital. (b) A schematic picture of relative energy of Ta_3N_5, O_2 and OH is shown. The impurity state of Ta_3N_5 has higher energy than OH and O_2.

3.4 Conclusions

The mechanism for the ORR on Ta_3N_5(100) surfaces has been examined theoretically. Clean and O-substituted surfaces were modelled to examine the relationship between the surface structures and catalytic activities. First, the adsorption structures and energies of oxygen were examined to clarify the mechanism for the ORR. From our calculations, it can be concluded that there are two possible adsorption structures of oxygen: Yeager-type and Griffiths-type. Energy diagrams for both the 4-electron and 2-electron reactions on both clean and O-substituted surfaces were then examined. By comparing each reaction, H_2O/H_2O_2 desorption was determined as the rate-determining step on both clean and O2-substituted surfaces. The difference in the catalytic activity of the clean and O2-substituted surfaces is mainly due to O_2 adsorption energy, and the O2-substituted surface is considered to have higher catalytic activity. Finally, we analysed the energy level of the impurity state for the O2-substituted surface and the orbital energies of adsorbed species. Based on the results, we have demonstrated the possibility of catalytic activity control by changing the surface structures. Control of the energy of the impurity state just above the SOMO level of O_2 is an effective way to improve catalytic activity for the ORR, and we have suggested C-doped $Ta_3N_{5-x}O_x$ as candidates for higher catalytic ORR activity. The concepts presented here are fundamental and useful for the design of new materials with higher catalytic activities.

References

(1) L. Carrette, K. a Friedrich and U. Stimming, *Fuel Cells*, 2001, **1**, 5.

(2) J. K. Nørskov, J. Rossmeisl, a. Logadottir, L. Lindqvist, J. R. Kitchin, T. Bligaard and H. Jónsson, *J. Phys. Chem. B,* 2004, **108**, 17886.

(3) V. Tripković, E. Skúlason, S. Siahrostami, J. K. Nørskov and J. Rossmeisl, *Electrochim. Acta*, 2010, **55**, 7975.

(4) M. J. Janik, C. D. Taylor and M. Neurock, *J. Electrochem. Soc.*, 2009, **156**, B126.

(5) A. Panchenko, M. T. M. Koper, T. E. Shubina, S. J. Mitchell and E. Roduner, *J. Electrochem. Soc.*, 2004, **151**, A2016.

(6) F. Jaouen, E. Proietti, M. Lefèvre, R. Chenitz, J.-P. Dodelet, G. Wu, H. T. Chung, C. M. Johnston and P. Zelenay, *Energy Environ. Sci.*, 2011, **4**, 114.

(7) U. Paulus, A. Wokaun, G. Scherer, T. Schmidt, V. Stamenkovic, V. Radmilovic, N. Markovic, and P. Ross, *J. Phys. Chem. B*, 2002, **106**, 4181.

(8) J. Greeley, I. E. Stephens, A. S. Bondarenko, T. P. Johansson, H. A. Hansen, T. F. Jaramillo, J. Rossmeisl, I. Chorkendorff, and J. K. Nørskov, *Nat. Chem*, 2009, **1**, 552.

(9) K. Kuttiyiel, K. Sasaki, Y. Choi, D. Su, P. Liu, and R. Adzic, *Nano Lett*., 2012, 12, 6266.

(10) W. Yang, Y. Wang, J. Li, and X. Yang, *Energy Environ. Sci*., 2009, **3**, 144.

(11) X. Chen, S. Sun, X. Wang, F. Li and D. Xia, *J. Phys. Chem. C*, 2012, **116**, 22737.

(12) G. Wu, K. L. More, C. M. Johnston and P. Zelenay, *Science*, 2011, **332**, 443.

(13) S. Gupta, D. Tryk, I. Bae, W. Aldred and E. Yeager, *J. Appl. Electrochem*., 1989, **19**, 19.

(14) R. Jasinski, *Nature*, 1964, **201**, 1212.

(15) M. Kaukonen, R. Kujala and E. Kauppinen, *J. Phys. Chem. C*, 2012, **116**, 632.

(16) B. Shan and K. Cho, *Chem. Phys. Lett*., 2010, **492**, 131.

(17) H. Niwa, K. Horiba, Y. Harada, M. Oshima, T. Ikeda, K. Terakura, J. Ozaki and S. Miyata, *J. Power Sources*, 2009, **187**, 93.

(18) K. Gong, F. Du, Z. Xia, M. Durstock and L. Dai, *Science*, 2009, **323**, 760.

(19) M. Lefèvre, E. Proietti, F. Jaouen and J.-P. Dodelet, *Science*, 2009, **324**, 71.

(20) Y. Okamoto, *J. Phys. Chem. C*, 2008, **112**, 5888.

(21) A. Lyalin, A. Nakayama, K. Uosaki and T. Taketsugu, *J. Phys. Chem. C*, 2013, **117**, 21359.

(22) J. Suntivich, H. A. Gasteiger, N. Yabuuchi, H. Nakanishi, J. B. Goodenough and Y. Shao-Horn, *Nat. Chem*., 2011, **3**, 546.

(23) A. Ishihara, Y. Ohgi, K. Matsuzawa, S. Mitsushima and K. Ota, *Electrochim. Acta*, 2010, **55**, 8005.

(24) R. Ohnishi, K. Takanabe, M. Katayama, J. Kubota and K. Domen, *J. Phys. Chem. C*, 2013, **117**, 496.

(25) A. Ishihara, M. Tamura, K. Matsuzawa, S. Mitsushima and K. Ota, *Electrochim. Acta*, 2010, **55**, 7581.

(26) R. Ohnishi, M. Katayama, K. Takanabe, J. Kubota and K. Domen, *Electrochim. Acta*, 2010, **55**, 5393.

(27) A. Ishihara, Y. Shibata, S. Mitsushima and K. Ota, *J. Electrochem. Soc.*, 2008, **155**, B400.

(28) A. Ishihara, S. Doi, S. Mitsushima and K. Ota, *Electrochim. Acta*, 2008, **53**, 5442.

(29) R. Ohnishi, Y. Takahashi, A. Takagaki, J. Kubota and K. Domen, *Chem. Lett.*, 2008, **37**, 838.

(30) S. Doi, A. Ishihara, S. Mitsushima, N. Kamiya and K. Ota, *J. Electrochem. Soc*., 2007, **154**, B362.

(31) J.-H. Kim, A. Ishihara, S. Mitsushima, N. Kamiya and K.-I. Ota, *Electrochim. Acta*, 2007, **52**, 2492.

(32) A. Ishihara, K. Lee, S. Doi, S. Mitsushima, N. Kamiya, M. Hara, K. Domen, K. Fukuda and K. Ota, *Electrochem. Solid-State Lett.*, 2005, **8**, A201.

(33) J. Seo, D. Cha, K. Takanabe, J. Kubota and K. Domen, *ACS Catal.*, 2013, **3**, 2181.

(34) J. Seo, D. Cha, K. Takanabe, J. Kubota and K. Domen, *Chem. Commun. (Camb).*, 2012, **48**, 9074.

(35) K. Ota, Y. Ohgi, K.-D. Nam, K. Matsuzawa, S. Mitsushima and A. Ishihara, *J. Power Sources*, 2011, **196**, 5256.

(36) K. Maeda and K. Domen, *J. Phys. Chem. C*, 2007, **111**, 7851.

(37) M. Hara, G. Hitoki, T. Takata, J. N. Kondo, H. Kobayashi and K. Domen, *Catal. Today*, 2003, **78**, 555.

(38) G. Hitoki, A. Ishikawa, T. Takata, J. N. Kondo, M. Hara and K. Domen, *Chem. Lett.*, 2002, **31**, 736.

(39) W.-J. Chun, A. Ishikawa, H. Fujisawa, T. Takata, J. N. Kondo, M. Hara, M. Kawai, Y. Matsumoto and K. Domen, *J. Phys. Chem. B*, 2003, **107**, 1798.

(40) E. Watanabe, H. Ushiyama and K. Yamashita, *Chem. Phys. Lett.*, 2013, **561-562**, 57.

(41) J. Wang, W. Luo, J. Feng, L. Zhang, Z. Li and Z. Zou, *Phys. Chem. Chem. Phys*., 2013, **15**, 16054.

(42) J. Wang, T. Fang, L. Zhang, J. Feng, Z. Li and Z. Zou, *J. Catal.*, 2014, **309**, 291.

(43) J. M. Soler, E. Artacho, J. D. Gale, A. García, J. Junquera, P. Ordejón and D. Sánchez-Portal, *J. Phys. Condens. Matter*, 2002, **14**, 2745.

(44) B. Hammer, L. Hansen and J. Nørskov, *Phys. Rev. B*, 1999, **59**, 7413.

(45) J. Junquera, Ó. Paz, D. Sánchez-Portal and E. Artacho, *Phys. Rev. B*, 2001, **64**, 1.

(46) N. Troullier and J. L. Martins, *Phys. Rev. B*, 1991, **43**, 1993.

(47) D. Sheppard, R. Terrell and G. Henkelman, *J. Chem. Phys.*, 2008, **128**, 134106.

(48) N. González-García, J. Pu, À. González-Lafont, J. M. Lluch and D. G. Truhlar, *J. Chem. Theory Comput.*, 2006, **2**, 895.

(49) T. Ohto, I. Rungger, K. Yamashita, H. Nakamura and S. Sanvito, *Phys. Rev. B*, 2013, **87**, 205439.

(50) H. J. Monkhorst and J. D. Pack, *Phys. Rev. B*, 1976, **13**, 5188.

(51) N. E. Brese, M. O'Keeffe, P. Rauch and F. J. DiSalvo, *Acta Crystallogr. Sect. C Cryst. Struct. Commun.*, 1991, **47**, 2291.

(52) P. W. Atkins, Physical Chemistry, 6th ed., 1998.

(53) Á. Valdés, Z. Qu, G. Kroes, J. Rossmeisl, and J. Nørskov, *J. Phys. Chem. C*, 2008, **112**. 9872

(54) P. Liao, J. Keith, and E. Carter, *J. Am. Chem. Soc*., 2012. **134**, 13296

Chapter 4

Interfacial structure and band diagram of n-type Ta_3N_5/water for photoelectrochemical water oxidation

4.1 Introduction

Photoelectrochemical production of hydrogen by splitting water is efficient and sustainable way for the utilization of solar energy. Water oxidation (R1) is anodic reaction that has non-zero overpotential even on the efficient electrocatalysts such as RuO_2 and IrO_2,[1,2]

$$2H_2O + 4h^+ \rightarrow O_2 + 4H^+ . \qquad \text{(R1)}$$

A thermodynamic requirement for water oxidation is the position of valence band (VB); VB of semiconductor materials is situated below a redox potential of O_2/H_2O. Compared to photocatalytic water-splitting, photoelectrochemical reaction has advantages of separating the reaction sites of hydrogen evolution and oxygen evolution and controlling Fermi energy of semiconductor by electrode potential. Tantalum nitride (Ta_3N_5) is one of the most promising materials as a photoanode for water-splitting.[3-5] To lower the overpotential of water oxidation reaction, in addition to lower the activation energy of the reaction itself, suppressing the recombination of excited charge carriers (electrons and holes) is of great importance. A Schottky-type barrier is typically significant for separating excited charge carriers in semiconductor electrode. For example, the band bending of semiconductor/co-catalyst heterojunction such as RuO_2/ZnO and RuO_2/TiO_2 was examined experimentally to show the existence of Schottky barrier at the interface with enhanced photocatalytic activity.[6,7] Moreover, some heterogeneous characters at the interface such as a mixed phase of TiO_2[8], and mixed domain of Ta_3N_5[9] also contribute to the improved activity because of the interfacial band diagram that accelerates the charge separation. In case of semiconductor/electrolyte system, band bending is also said to be formed and the thermodynamic factors regarding the magnitude of the band bending can shift the on-set potential for water oxidation[10].

To utilize Ta_3N_5 as a photoanode, efforts to improve the activity have been focused on increasing photo absorption property[11,12], improving the crystallinity[13], modifying surface and contact to co-catalyst.[14,15] The surface reactions of oxygen adsorption,[16] water adsorption,[17] and oxygen reduction[18] have been also reported. However, fewer attention has been paid to semiconductor/electrolyte interface except flat band (FB) potential measured by Mott-Schottky plots[5,12,14] The examined FB potential varies according to studies; one examined FB potential of -0.5 V vs. NHE together with conduction band (CB) and VB positions of -0.5 and 1.6 V vs. NHE[12], or another examinations addressed FB potential of -0.5 V vs. RHE[14] and 0.0 V vs. NHE[5] respectively. However, how FB potential can be situated above or equal to CB has not been mentioned in these studies. In addition, interestingly, Nurlaela et al pointed out that the only topmost modification of Ta_3N_5 change the FB potential[14]. These studies confirm a necessity of obtaining the energy diagram at the interface again.

In this chapter, band diagram of Ta_3N_5/water in electrochemical condition is presented. Especially, whether band edge pinning or Fermi level pinning occurs is examined by first principles calculation combined with double reference method[19]. Ta_3N_5 is, in general, n-type semiconductor with O-enriched and N-defect structure[20]. From thermodynamic analysis, the formation of O_N (N atom is substituted by O atom) is favorable in synthesis condition,[21] and the aqueous stability of Ta_3N_5 is also so poor that Ta_2O_5 is formed in a potential range between H^+/H_2 and O_2/H_2O in pH 0-14.[22] In addition, V_N (vacancy at N site) is formed as a result of self-oxidation in photocatalytic process[23]. In our study, electrochemical condition is assumed as to get the equilibrium picture. Thereby, either bulk O_N or surface O_N is introduced as a model of n-type Ta_3N_5 with high and low dopant concentration respectively. In addition, band alignment can be easily affected by adsorbents such as O and OH. Therefore, n-type Ta_3N_5/water interfacial structure is examined from the view point of the amount of O_N and surface adsorbents first and then band diagram with the stable interfacial structure is investigated.

4.2 **Method**

DFT calculations were performed using the GPAW[24,25] code together with the ASE simulation package[26]. The GGA/PBE[27] functional and PAW method[28] were employed for all calculations, and the gpaw-setups-0.9.11271 was used for all elements. The size of optimized unit cell of Ta_3N_5 is a = 3.90 Å, b = 10.32 Å and c = 10.35 Å, which is in good agreement with previously reported experimental values[20] (a = 3.89 Å, b = 10.22 Å and c = 10.27 Å). As the surface models, (100) surface is selected because it is stoichiometric phase and having the lowest surface energy[16]. It should be noted that band position differs according to the surface orientation. Surface oriented behavior is also an important subject however it is out of the scope of this study. According to the purpose, we varied the size of the slab model; for the examination of the surface structure, asymmetric (3×1×1) supercell consisting of 96 atoms with at least 14 Å vacuum region was used. For the examination of the band positions, asymmetric (6×1×1) supercell is needed because band position shows relatively slow convergence on the size of the slab model. Finally, on the examination of electrode potential dependent behavior of Ta_3N_5, ice-like water molecules are explicitly introduced in the asymmetric (6×1×1) supercell. In order to shift the Fermi energy, i.e. electrode potential, double reference method is employed. The method requires to introduce additional charges with uniform background counter-charge. In that case, the symmetric (6.5×1×1) supercell is employed to avoid the unphysical behavior of added charge in a system. We confirmed that the symmetric (6.5×1×1) supercell and symmetric (13×1×1) supercell exhibit almost the same diagram under neutral condition in an inner 20 Å area from Ta_3N_5 surface.

The electronic structures were calculated by the finite difference method with a grid parameter of approximately 0.18 Å and with a k-point sampling on a (1×3×3) grid for the slab in a vacuum system. For the calculation of the slab in aqueous system, the grid parameter of 0.2 Å and k-point sampling on a (1×2×2) is used to reduce the computational cost. The systems with and without water is optimized until the maximum force on atoms was smaller than 0.1 eV/ Å and 0.05 eV/ Å respectively. The dipole correction is applied in asymmetric systems. The Hubbard *U* parameter is added for the calculation of the band alignments and diagrams. The *U* parameter is determined to be 2.0 eV for Ta atoms by linear response method[29] that cancels the self-interaction error. We confirm that although we use *U*=5.0 eV where calculated band gap matches the experimental one, the position of valence band maximum does not change because VB is mainly consists of N 2p orbitals. Thus, although *U* value of 2.0 eV still underestimates the band gap to be 1.68 eV (exp. 2.1 eV[4]), the position of VB is little influenced by the band gap error.

4.3 Results and discussion

4.3.1 Surface structure of n-type Ta_3N_5 in water

A. Surface O_N Ta_3N_5 model

As low dopant model, surface O_N model is employed. Supposing that the introduction of O_N is associated with the electrochemical production of nitrogen or ammonia in aqueous condition,

$$Ta_3N_5 + xH_2O \rightarrow Ta_3N_{5\text{-}x}O_x + 2xH^+ + 2xe^- + x/2\ N_2 \quad (N_2 \text{ production}) \qquad \text{(R2)}$$

$$Ta_3N_5 + xH_2O + xH^+ + xe^- \rightarrow Ta_3N_{5\text{-}x}Ox + xNH_3 \quad (NH_3 \text{ production}). \quad \text{(R3)}$$

The stabilities of the O_N surfaces in electrochemical condition are evaluated by calculating the reaction energies as follows

$$\Delta G_{N_2} = G(Ta_3N_{5\text{-}x}O_x) + x/2\ G(N_2) + \mu_{H^+ + e^-} - x/2\ G(H_2O) - G(Ta_3N_5) \qquad (4.1)$$

$$\Delta G_{NH_3} = G(Ta_3N_{5\text{-}x}O_x) + x/2\ G(NH_3) - G(Ta_3N_5) - xG(H_2O) - \mu_{H^+ + e^-}\ . \qquad (4.2)$$

Here, computational hydrogen electrode is used for the evaluation of $\mu_{H^+ + e^-}$. As surface O_N models, 1 to 4 O_N per unit cell are introduced notated as 'nO_N surface' (n=1-4). These models are equivalent to the doping concentration of 9.4×10^{13} e/cm^{-2}, 1.9×10^{14} e/cm^{-2}, 2.8×10^{14} e/cm^{-2}, and 3.8×10^{14} e/cm^{-2} respectively. The position of O_N is determined as to be the most stable one on $1O_N$ and $2O_N$ surface models. In case of $3O_N$ surface, stable structure is searched by adding one O_N on the most stable $2O_N$ surface. The $4O_N$ surface is also determined by the similar way. Figure 4-1 shows the reaction energies as a function of electrode potential. Generally, ammonia is produced in negative potential region and nitrogen is produced in positive potential region. Thermodynamically, the increased number of O_N enhances more stability. This result is somewhat consistent to previous study that bulk Ta_2O_5 is thermodynamically more stable than to bulk Ta_3N_5 in water.[22] In reality, making O_N impurity is not only controlled by the reaction energy but also by its kinetics. With the intention of demonstrating interfacial structures and band diagrams of n-type Ta_3N_5, $2O_N$ and $4O_N$ surfaces are selected for further investigations.

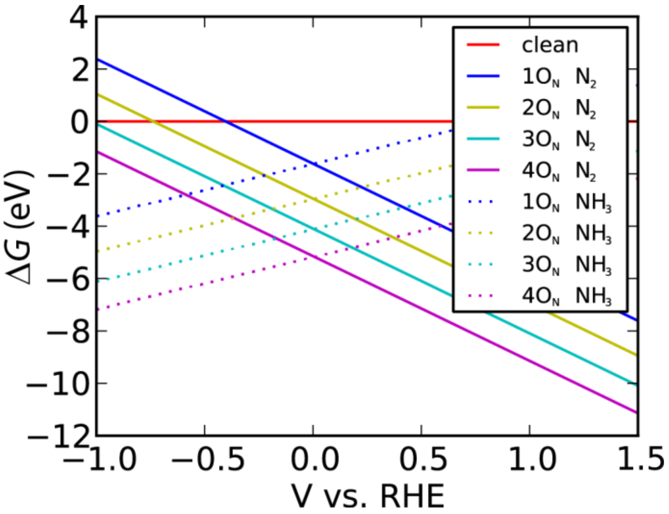

Figure 4-1. Reaction energy of N_2 (solid line) and NH_3 (dotted line) production to form surface-nO_N (n=1-4) structures. Purple lines are locating at the bottom in all potential region, indicating $4O_N$ surface is the most stable.

In addition to the analysis on the amount of surface O_N, adsorbents at a given electrode potential is examined because large part of surface area is considered to be covered by stable adsorbents of OH and O. Here, we will notate '*' for adsorbents. We assume these adsorbents are generated by the reaction with water such as

$$\text{surface} + H_2O \rightarrow \text{surface-OH} + H^+ + e^- \qquad \text{(R4)}$$

$$\Delta G_{OH} = G(\text{surface-OH}) + \mu_{H^+ + e^-} - G(\text{surface}) - G(H_2O) \qquad (4.3)$$

and

$$\text{surface} + H_2O \rightarrow \text{surface-O} + 2H^+ + 2e^- \qquad \text{(R5)}$$

$$\Delta G_O = G(\text{surface-O}) + 2\mu_{H^+ + e^-} - G(\text{surface}) - G(H_2O). \qquad (4.4)$$

The coverage of O* and OH* is limited to 0.94-1.87 molecule nm^{-2} in our models. The reaction Gibbs energy is also dependent on the electrode potential. The results are summarized as surface phase diagrams as shown in Figure 4-2. On clean surface (Figure 4-2(a)), surface with OH*, O*+OH*, and 2O* are stable below -0.5 V vs. RHE, in the range of -0.5 V- 0.6 V vs. RHE, and above 0.6 V vs. RHE respectively. On the other hand, on $2O_N$ surface (Figure 4-2 (b)), surface with 2OH* is always most stable. On $4O_N$ surface (Figure 4-2 (c)), surface structure switches from the one with 2OH* to 2O* at -0.3 eV. On OER potential region, i.e. 1.5 V vs. RHE (1.23 V + overpotential), surface with 2O*, 2OH*, and 2O* on clean, $2O_N$, and $4O_N$ surfaces are detected respectively. The reason for stable surface with 2O* on clean surface can be explained as follows. On clean surface, O_2 molecules cannot adsorb and O adsorbed structure is unstable without surface corruption or re-construction. Thus, on the surface with 2O* model, the bindings of two O atoms cause the displacement of surface N atoms. As a result, one stable N-N pairs per unit cell is formed at the surface with the bond length of 1.25 Å. We will mention about it later again. On the other hand, the trend lying on O_N surfaces can be explained by the tendency of binding energy of oxygen molecule and OH. From Chapter 3, both binding energies of O_2 and OH increase as the number of O_N impurity increases. The increase of OH binding energy is smaller than that of O_2 adsorption energy, thus, surface with O* are getting prior rather than surface with OH* as O_N increases.

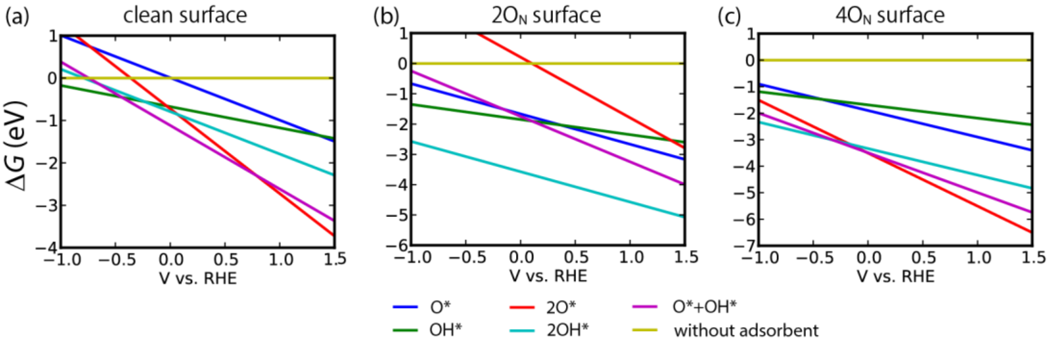

Figure 4-2. Reaction energies of OH and O adsorption (R4 and R5) on (a) clean surface, (b) $2O_N$ surface, and (c) $4O_N$ surface. Colors indicate adsorbates on the surface.

B. Bulk O_N Ta_3N_5 model

Bulk O_N Ta_3N_5 model is considered as high dopant model in synthesized condition. Here, bulk O_N is introduced as to match the experimentally reported ratio of O and N; replacement of one N atom to one O atom in the unit cell gives rise to a composition of $Ta_3N_{4.75}O_{0.25}$, which is similar to experimentally obtained composition of $Ta_3N_{4.80}O_{0.20}$.[20] A position of O_N is determined thermodynamically and we get a structure with a bulk O_N at the 3-coordinate N site. The lattice constant of bulk O_N composition is a = 3.91 Å, b = 10.28 Å and c = 10.36 Å which is very similar to that of perfect Ta_3N_5 except 0.4 % reduction of *b*-axis. The surface based on this composition is notated as 'bulk-O_N surface'. The position of O_N and the trend of lattice constant reduction on *b*-axis are also consistent with the experimental results.[20] Similar to low dopant model, equilibrium structure of surface adsorbents in electrochemical environment is determined as shown in Figure 4-3. From these calculations, surface adsorbents switches from 2OH* to O*+OH* at 1.24 V vs. RHE. The potential is almost the same as the redox potential of O_2/H_2O. Thus, both 2OH* and O*+OH* are employed for further investigations.

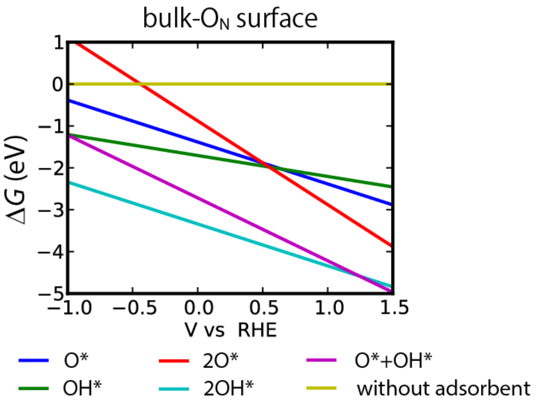

Figure 4-3. Reaction energies of OH and O adsorption (R4 and R5) on bulk-O_N surface.

4.3.2 Band alignment of n-type Ta_3N_5 as a function of surface structure

As discussed above, under the applied potential, O_N impurities and adsorptions of O and OH are induced at the interface. In this section band positions of n-type Ta_3N_5 as well as the positions of surface states and Fermi energy on various surface structures are examined to discuss how O_N impurities and adsorptions affect the band diagram of Ta_3N_5 in vacuum.

The position of the Fermi energy needs to be determined with some cares by DFT calculations to connect calculation models to the systems in electrochemical environment. The Fermi energy in semiconductor is the charge neutral level which is in one-on-one correspondence with electrode potential. The Fermi energy in intrinsic semiconductor is determined by the position and density of state (DOS) of CB and VB,

$$E_F = \frac{1}{2}(E_v + E_c) + \frac{1}{2}k_B T \ln\frac{N_v(T)}{N_c(T)} \tag{4.5}$$

where E_v and E_c are the energy of VB maximum (VBM) and CB minimum (CBM), N_v and N_c are effective density of states of VB and CB. The effective density of states can be calculated with the results of DFT, i.e.

$$N_v(T) = \int_{-\infty}^{Ev} n_v(E) e^{-\frac{E_v - E}{k_B T}} dE \tag{4.6}$$

$$n_v(E) = D_v(E)/V \tag{4.7}$$

$$N_c(T) = \int_{E_c}^{\infty} n_c(E) e^{-\frac{E - E_c}{k_B T}} dE \tag{4.8}$$

$$n_c(E) = D_c(E)/V \tag{4.9}$$

where D_v and D_c are density of states and V is the volume of the unit cell. To avoid the contribution from the fixed atoms in the slab, only density of states projected on the relaxed part of the slab is used. In case of n-type semiconductor, Fermi energy is also determined as to satisfy the charge neutrality.[30] In that case, formula of Fermi energy is classified into two according to the position of donor level induced by dopants. In case that Fermi level is locating at the surface state or above CBM with an order of $k_B T \approx 0.025$ eV (T=300 K), Fermi level is determined as a directly calculated value. On the other hand, if the position of CBM and donor level is very close within an order of $k_B T$, Fermi energy should be calculated as

$$E_F = E_c + k_B T \ln \frac{N_d}{N_c} \tag{4.10}$$

where N_d is a dopant density. However, such small doping density cannot be captured by our calculations because of the size of the unit cell and the accuracy of the calculation of the charge. Fortunately, the situation of using (4.10) does not occur in our calculations.

The calculation of Fermi level depends on DOS. Therefore, it depends on the size of the slab model because the size determines the weight of surface states on DOS. When we use DOS projected onto the relaxation part of the slab, its surface area is 87.7 m^2 g^{-1} on clean surface. Experimentally synthesized Ta_3N_5 nanocrystal has the surface area of about 60 m^2 g^{-1}.[14,31] Thus, weight of surface state is reasonable in our model.

A. Surface O_N Ta_3N_5 model

Using Fermi energy derived by above method, the band diagrams of clean and surface-O_N models are calculated first as a means of the local density of states (LDOS) shown in Figure 4-4.

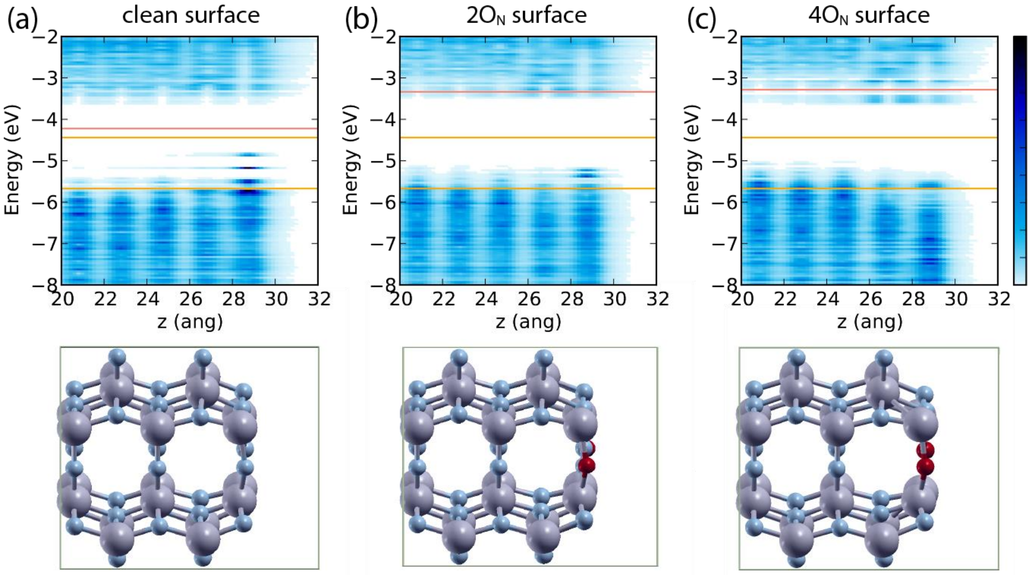

Figure 4-4. Band diagrams and surface geometry of (a) clean surface, (b) $2O_N$ surface, and (c) $4O_N$ surface in vacuum with its geometry. Only five-topmost layers with vacuum region are shown. A vacuum energy is set to be a reference. An upper yellow line at 4.44 eV is a redox potential of H^+/H_2 and a lower line at 5.67 eV is a redox potential of O_2/H_2O. Red lines indicate Fermi energy in each figures.

On clean surface, surface dangling bond state lies above VBM and Fermi level lies between the top of dangling bond level and CBM. The clean surface is an intrinsic semiconductor and the position of VBM in bulk region almost matches the redox potential of O_2/H_2O. On the other hand, $2O_N$ and $4O_N$ surfaces are n-type semiconductor and Fermi energy is locating in the CB. The positions of VB and CB are almost the same in $2O_N$ and $4O_N$ surfaces and only 0.1 eV shift is observed. In addition, surface dangling bond states are disappeared because they are saturated by excess electrons donated by surface O_N impurities.[32]

Next, effects of adsorbents on band positions are examined. In Figure 4-5, band alignments obtained by LDOS calculations of surfaces without adsorbent, surface with OH*, with O*, surface detected at 1.23 V vs. RHE are shown. There exist surface states only on the clean surface regardless of adsorbents. Generally, adsorptions of OH and O induce the down shift of the band positions because negatively charged OH and O form dipole at the interface, whereas the reduction by OH is relatively small or negligible. The clean surface is an intrinsic semiconductor and Fermi energy lies between surface states and CBM or VBM. The position of surface states varies according to the surface adsorbent. The clean surface without any adsorbent and with OH* have surface states just above the VB, implying relatively high stabilities of theses surfaces. The surface states at clean surface with O* and 2O* come from N-N bonding or anti-bonding state as is shown in Figure 4-6. The adsorption of O atoms with negative charge means that the adsorption donates hole to Ta_3N_5. Thus, clean surface adsorbed by O atoms show p-type semiconductor. The hole is distributed at surface N atoms and strengths N-N bonding. This situation can be translated into the self-oxidation process of photocatalytic water oxidation,

$$2N^{3-} + 6h^{+} \rightarrow N_2 . \qquad \text{(R6)}$$

The band alignments of $2O_N$ surfaces with 2OH* and with O*, and $4O_N$ surface with 2O* also show similar behavior. Because formal valences of adsorbed OH and O are -1 and -2 respectively, the intrinsic nature of semiconductor is recovered on these surfaces. Although the density of O_N impurity in our models is much less than that of experimentally reported one, our results indicate the reduction of doping density induced by the adsorbents. It could explain the reduction of carrier density in porous structure.[33]

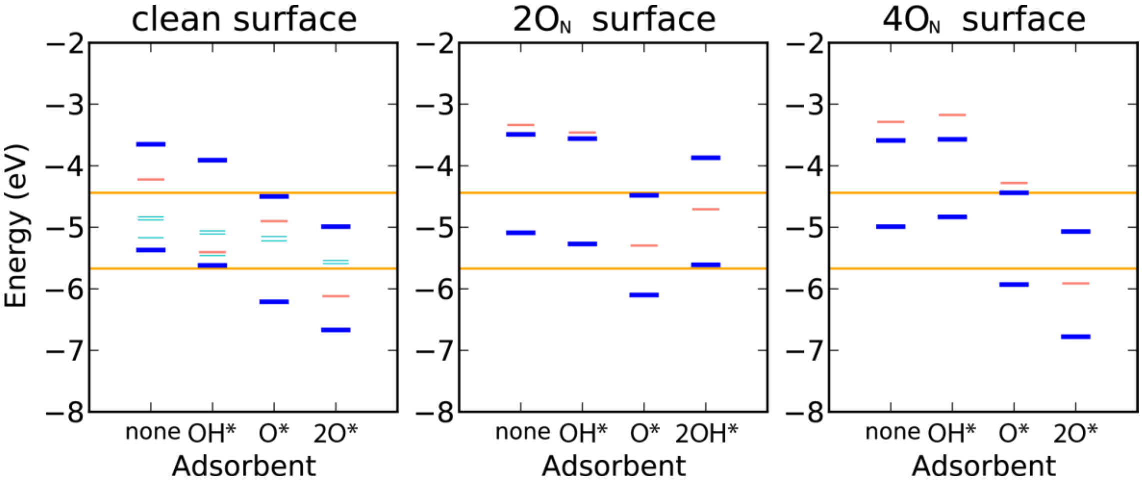

Figure 4-5. Band alignments of clean, $2O_N$, and $4O_N$ surfaces together with adsorbents. Blue, red, yellow, and cyan lines indicate VBM and CBM, Fermi energy, redox potentials of H^+/H_2 and O_2/H_2O, and surface states respectively.

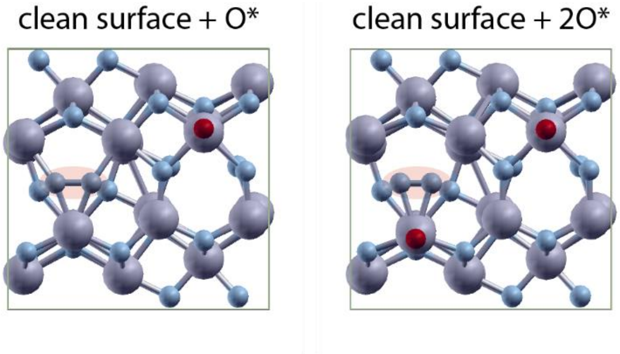

Figure 4-6. Surface structures of clean surface with one or two O* atoms. Dark purple, blue, and red balls indicate Ta atoms, N atoms, and O atoms respectively. Two N atoms are highlighted to clearly show a formation of N-N bond.

B. Bulk O_N Ta_3N_5 model

Band alignments of bulk-O_N surface with adsorbents are calculated and shown in Figure 4-7. The surfaces with 2OH* and O*+OH* are also shown because these are stable around 1.23 V vs. RHE. On bulk-O_N surfaces, similar trend can be seen; the adsorptions of OH and O induce the down shift of band positions. Clearly, the position of VB in bulk-O_N is lower than those in clean surface, and is always situated below the redox potential of O_2/H_2O regardless of adsorbents, which indicates the availability of $Ta_3N_{2.75}O_{0.25}$ for water oxidation. It should be noted that the previous DFT calculations on 0.83-2.50 % O-enriched $Ta_3N_{5-x}O_x$, or O-enriched and Ta-vacant $Ta_{2.91}N_{4.58}O_{0.41}$ show similar down shift of the band position,[12,21] while $Ta_3N_{4.83}O_{0.25}$ shows the upper shift of the band position.[12] Because the band positions are sensitive to dipole, only a slight change of non-stoichiometry results in either upper shift or down shift of the positions.

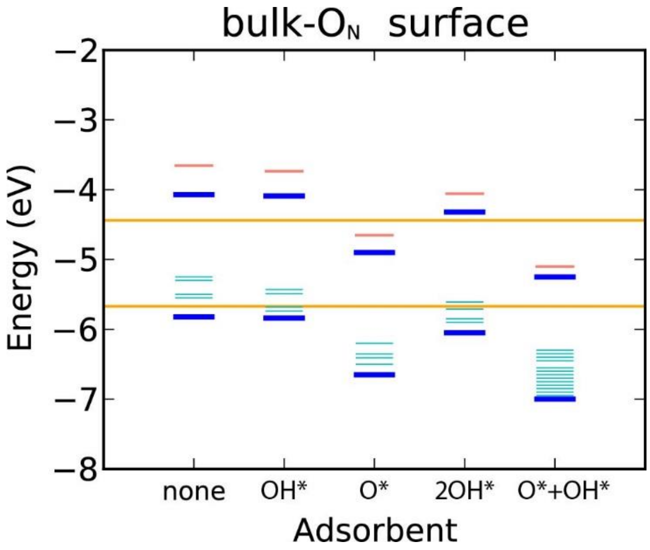

Figure 4-7. Band alignments of bulk-O_N surface together with adsorbents. Blue, red, yellow, and cyan lines indicate VBM and CBM, Fermi energy, redox potentials of H^+/H_2 and O_2/H_2O, and surface states respectively.

4.3.3 **Band diagram of n-type Ta_3N_5/water interface in electrochemical system**

With the purpose of revealing 'in situ' behavior of hole transfer, the band diagrams of n-type Ta_3N_5/water interfaces in aqueous solution as a function of electrode potential are investigated. Especially, whether band edge pinning (BEP) or Fermi level pinning (FLP) occurs are discussed in this section by using bulk-O_N surface model because its composition is similar to experimentally obtained one. The electrode potential is calculated by Fermi energy referring H^+/H_2 redox potential relative to vacuum level,

$$\phi = -4.44 - \phi_{Fermi} \tag{4.11}$$

where ϕ is the electrode potential and ϕ_{Fermi} is Fermi energy relative to vacuum level. The systems with excess charge were optimized by relaxing adsorbents and water molecules except 'reference water' near the boundary. Because surface with 2OH* and surface with O*+OH* are detected below and above 1.24 V vs. RHE respectively, the electrode potential of these two surfaces are varied and connected at 1.24 V. In our calculations, Schottky-type barrier (SB) is observed because of the charge transfer from the semiconductor to water. Now we can define four properties; energy of the valence band in bulk (E_V), energy of the valence band at the surface (E_{VS}), semiconductor barrier height (V_{SC}), and Fermi energy. An example of band diagram having SB is shown in Figure 4-8.

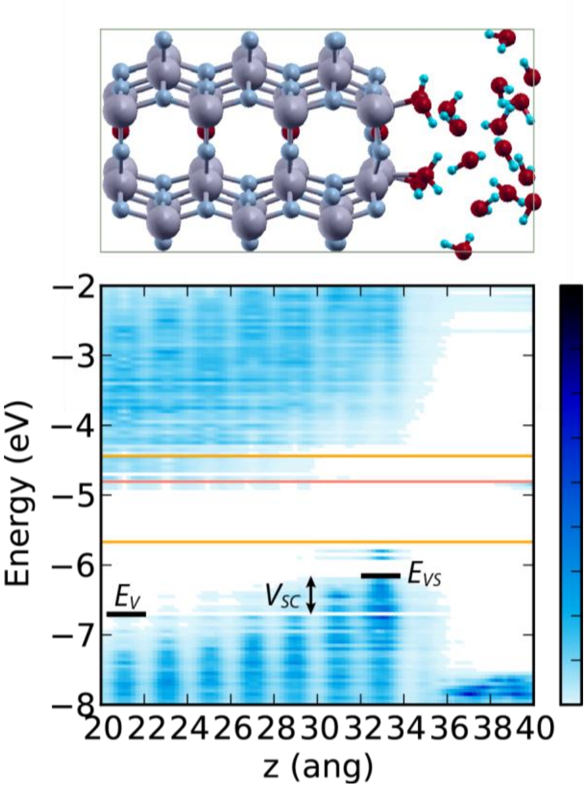

Figure 4-8 Band diagram and geometry of bulk-O_N surface with 2OH* with excess charge of 2.5*e* in calculated cell. A vacuum energy is set to be a reference. An upper yellow line at 4.44 eV is a redox potential of H^+/H_2 and a lower line at 5.67 eV is a redox potential of O_2/H_2O. A red line indicates Fermi energy.

By varying excess charges on surfaces, we get the full picture of band diagram which are summarized in Figure 4-9. Depending on how E_{V}, E_{VS}, and V_{SC} shift, the mechanism can be classified into three cases by the values of the electrode potential. Below 0.73 V vs. RHE (region I in Figure 4-9), E_{V} shifts downward linearly as electrode potential increase with a slope of 0.83. Accordingly, E_{VS} also shifts downwards as electrode potential increase, however, its slope is 0.41 and smaller than that of E_{V}. The slope of 0.41 means the diagram at the interface shows intermediate behavior between BEP and FLP; the BEP is the limit of the slope of 1.0 and the FLP is the limit of the slope of 0.0. The FB potential of -0.8 V vs. RHE is obtained as to satisfy $V_{\mathrm{SC}}=0$ by fitting V_{SC} with a linear function, which agree well with experimental values of -0.5 V – 0.0 V vs. RHE.[5,12,14]

In region between 0.73 V – 1.10 V vs. RHE (region II in Figure 4-9), Fermi energy shifts from the bottom of CB to surface state just above VB. The down shift across the band gap means the reduction of doping density to be nearly zero. Because the intrinsic semiconductor does not show SB, the reduction of V_{SC} occurs at this region.

Above 1.10 V vs. RHE (region III in Figure 4-9), the picture is dramatically changed. In this region, E_{V} remains almost constant, while E_{VS} and V_{SC} are lowered. Fermi level is pinned at the surface states just above E_{VS}. Therefore surface-state induced Fermi level pinning is dominating in this region. The system is not n-type semiconductor anymore. As a character of p-type comes to be prior, V_{SC} reduces to be negative value, forming downward band bending.

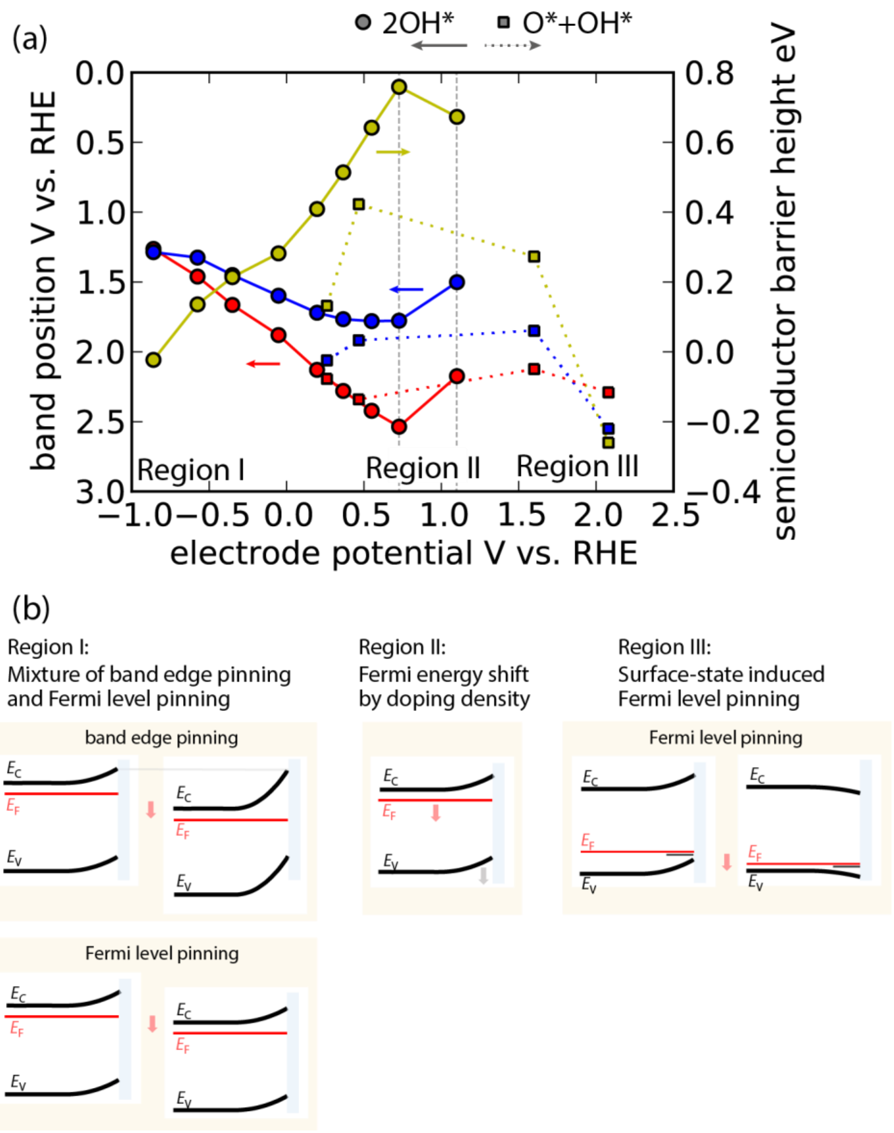

Figure 4-9 (a) Band diagrams as a function of electrode potential. Position of E_V and E_{VS} are shown in red and blue lines referring left y-axis, and V_{SC} are shown in yellow line referring right y-axis. The solid line and circular marks refers the results from surface with 2OH* structure. The dashed line and tetragonal marks refers the results from surface with O* and OH* structure. The grey dashed line at 1.24 V vs. RHE indicates the potential where surface phase is changed. (b) Overview of band diagram for n-type Ta_3N_5/water interface.

Finally, guideline to efficient charge separation is discussed. As already pointed out, FLP at photoanode/water interface is insufficient in that the driving force for charge separation cannot be fully gained by the potential increase.[10] The slope of 0.41 on V_{SC} in region I implies the intermediate bahevior between FLP and BEP; only half of potential shift contributes to the formation of SB. To clearly show the origin of FLP, changes in the electron density and electrostatic potential between -0.86 V vs. RHE and 0.73 V vs. RHE are calculated. In Figure 4-10(b), the positive red area represent an electron accumulation region and negative blue area represent an electron reduction region. As electrode potential is increased, the electron reduction occurs in wide area of Ta_3N_5 (20 Å < z < 33 Å) and local interfacial region (34 Å < z < 35 Å). Accordingly, the reduction of change in the electrostatic potential occurs at the same region in Figure 4-10(c). Suppose full BEP is the limit where all the changes in the electron density and electrostatic potential occur in Ta_3N_5 region whereas full FLP is the limit where all the changes occur at the interface, partial redistribution of electrons at the interface is the origin of FLP at the Ta_3N_5/water interface. It is evident that such charge redistribution is related to the existence of surface states and molecular orbitals of adsorbents perturbed by the interaction with the semiconductor surface. Without them, charge redistribution must occur in aqueous region or Ta_3N_5 bulk region, leading to getting rid of FLP. However, these states or orbitals cannot be completely removed, implying an intrinsic nature of partial FLP at the Ta_3N_5/water interface. Another insufficiency at Ta_3N_5/water interface is the reduction of V_{SC} above 0.73 V vs. RHE. This is due to the loss of n-type character of the system. Supposing Fermi energy lies in or below CB on n-type semiconductor, downshift of band positions has a positive effect for keeping n-type character at more positive electrode potential region. Consequently, surface modification is significant not only to shift the band positions but also to get a driving force for charge separations.

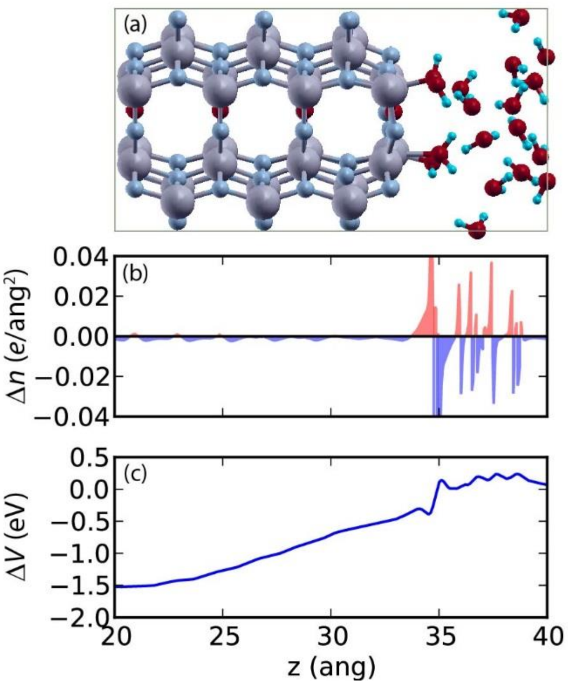

Figure 4-10 Changes in the electron density and electrostatic potential between -0.86 V vs. RHE and 0.73 V vs. RHE (a) Geometry of bulk-O_N surface with 2OH* in aqueous solution. (b) Change in the electron density; $\Delta n = n$(0.73 V vs. RHE)-n(-0.86V vs. RHE). The positive red area represent an electron accumulation region and the negative blue are represent an electron reduction region. (c) Change in the electrostatic potential; $\Delta V = V$(0.73 V vs. RHE)-V(-0.86V vs. RHE).

4.4 Conclusions

We have presented a band diagram of Ta_3N_5/water interface using DFT combined with double reference method. As n-type Ta_3N_5 models, surface O_N or bulk O_N is introduced. We first find the stable structure of each surface model in a view point of surface adsorbents. Then effect of adsorbents on band alignment is discussed. The adsorptions of O* and OH* negatively shift the band position and also change the doping density of Ta_3N_5. Finally, band diagrams of n-type

Ta_3N_5/water are obtained. In a lower potential region below 0.7 V vs. RHE, an intermediate behavior of band edge pinning and Fermi level pinning is observed. In region between 0.7 V – 1.1 V vs. RHE, simple Fermi level shift is occurred by the reduction of doping density. In higher potential region above 1.1 V vs. RHE, surface-state induced Fermi level pinning is observed. From our calculations, Schottky-type barrier height is dependent on electrode potential, and not sufficient because of Fermi level pinning and loss of n-type character. Through our studies on the band diagram of Ta_3N_5/water interface, intrinsic nature of insufficient partial Fermi level pinning are found. Also, surface modification is significant not only to shift the band positions but also to get a driving force for charge separations.

Reference

(1) C. C. L. McCrory, S. Jung, J. C. Peters and T. F. Jaramillo, *J. Am. Chem. Soc*., 2013, **135**, 16977.

(2) M. E. G. Lyons and S. Floquet, *Phys. Chem. Chem. Phys*., 2011, **13**, 5314.

(3) M. Hara, G. Hitoki, T. Takata, J. N. Kondo, H. Kobayashi and K. Domen, *Catal. Today*, 2003, **78**, 555.

(4) G. Hitoki, A. Ishikawa, T. Takata, J. N. Kondo, M. Hara and K. Domen, *Chem. Lett*., 2002, **31**, 736.

(5) W.-J. Chun, A. Ishikawa, H. Fujisawa, T. Takata, J. N. Kondo, M. Hara, M. Kawai, Y. Matsumoto and K. Domen, *J. Phys. Chem. B*, 2003, **107**, 1798.

(6) M. T. Uddin, Y. Nicolas, C. Olivier, L. Servant, T. Toupance, S. Li, A. Klein and W. Jaegermann, *Phys. Chem. Chem. Phys*., 2015, **17**, 5090.

(7)M. T. Uddin, Y. Nicolas, C. Olivier, T. Toupance, M. M. Müller, H. J. Kleebe, K. Rachut, J. Ziegler, A. Klein and W. Jaegermann, *J. Phys. Chem. C*, 2013, **117**, 22098.

(8) M. G. Ju, G. Sun, J. Wang, Q. Meng and W. Liang, *ACS Appl Mater Interfaces*, 2014, **6**, 12885.

(9) Y.-C. Wang, C.-Y. Chang, T.-F. Yeh, Y.-L. Lee and H. Teng, *J. Mater. Chem. A*, 2014, **2**, 20570.

(10) J. E. Thorne, S. Li, C. Du, G. Qin and D. Wang, *J. Phys. Chem. Lett*., 2015, **6**, 4083.

(11) J. Wang, A. Ma, Z. Li, J. Jiang, J. Feng and Z. Zou, *RSC Adv*., 2014, **4**, 55615.

(12) M. Harb, P. Sautet, E. Nurlaela, P. Raybaud, L. Cavallo, K. Domen, J. Basset and K. Takanabe, *Phys. Chem. Chem. Phys*., 2014, **16**, 20548.

(13) S. S. K. Ma, T. Hisatomi, K. Maeda, Y. Moriya and K. Domen, *J. Am. Chem. Soc*., 2012, **134**, 19993.

(14) E. Nurlaela, S. Ould-Chikh, M. Harb, S. del Gobbo, M. Aouine, E. Puzenat, P. Sautet, K. Domen, J.-M. Basset and K. Takanabe, *Chem. Mater*., 2014, **26**, 4812.

(15) S. Chen, S. Shen, G. Liu, Y. Qi, F. Zhang and C. Li, *Angew. Chemie. Int. Ed*, 2015, **54**, 3047.

(16) E. Watanabe, H. Ushiyama and K. Yamashita, *Chem. Phys. Lett*., 2013, **561-562**, 57.

(17) J. Wang, W. Luo, J. Feng, L. Zhang, Z. Li and Z. Zou, *Phys. Chem. Chem. Phys*., 2013, **15**, 16054.

(18) E. Watanabe, H. Ushiyama and K. Yamashita, *Catal. Sci. Technol*., 2015, **5**, 2769.

(19) C. D. Taylor, S. a. Wasileski, J. S. Filhol and M. Neurock, *Phys. Rev. B - Condens. Matter Mater. Phys*., 2006, **73**, 165402.

(20) S. J. Henderson and A. L. Hector, *J. Solid State Chem*., 2006, **179**, 3518.

(21) J. Wang, T. Fang, L. Zhang, J. Feng, Z. Li and Z. Zou, *J. Catal*., 2014, **309**, 291.

(22) K. A. Persson, B. Waldwick, P. Lazic and G. Ceder, *Phys. Rev. B*, 2012, **85**, 235438.

(23) D. Yokoyama, H. Hashiguchi, K. Maeda, T. Minegishi, T. Takata, R. Abe, J. Kubota and K. Domen, *Thin Solid Films*, 2011, **519**, 2087.

(24) J. J. Mortensen, L. B. Hansen and K. W. Jacobsen, *Phys. Rev. B - Condens. Matter Mater. Phys*., 2005, **71**, 035109.

(25) J. Enkovaara, C. Rostgaard, J. J. Mortensen, J. Chen, M. Dułak, L. Ferrighi, J. Gavnholt, C. Glinsvad, V. Haikola, H. A. Hansen, H. H. Kristoffersen, M. Kuisma, A. H. Larsen, L. Lehtovaara, M. Ljungberg, O. Lopez-Acevedo, P. G. Moses, J. Ojanen, T. Olsen, V. Petzold, N. A. Romero, J. Stausholm-Møller, M. Strange, G. A. Tritsaris, M. Vanin, M. Walter, B. Hammer, H. Häkkinen, G. K. H. Madsen, R. M. Nieminen, J. K. Nørskov, M. Puska, T. T. Rantala, J. Schiøtz, K. S. Thygesen and K. W. Jacobsen, *J. Phys. Condens. Matter*, 2010, **22**, 253202.

(26) S. R. Bahn and K. W. Jacobsen, *Comput. Sci. Eng*., 2002, **4**, 56.

(27) J. Perdew, K. Burke and M. Ernzerhof, *Phys. Rev. Lett*., 1996, **77**, 3865.

(28) P. E. Blöchl, *Phys. Rev. B*, 1994, **50**, 17953.

(29) M. Cococcioni and S. de Gironcoli, *Phys. Rev. B*, 2005, **71**, 035105.

(30) G. Grosso and G. P. Parravicini, Solid State Physics, 2000, Academic Press

(31) X. Liu, L. Zhao, K. Domen and K. Takanabe, *Mater. Res. Bull.*, 2014, **49**, 58.

(32) Y. Huang, C. Ling, M. Jin, J. Du, T. Zhou and S. Wang, *Phys. Chem. Chem. Phys*., 2013, **15**, 17804.

(33) A. Ziani, E. Nurlaela, D. S. Dhawale, D. A. Silva, E. Alarousu, O. F. Mohammed and K. Takanabe, *Phys. Chem. Chem. Phys*., 2015, **17**, 2670.

Chapter 5

Atomic-scale analysis of the RuO_2/water interface under electrochemical conditions

5.1 Introduction

Ruthenium oxide has been widely studied as an electrode material because of its potential application in electrocatalysts[1–11] and energy storage supercapacitors.[12–18] As an example, when employed in electrocatalysis, RuO_2 exhibits high catalytic activity for the oxidation of hydrogen chloride[1–5] as well as for the oxygen evolution[6–9] and carbon dioxide reduction reactions.[10,11] However, to increase its electrocatalytic activity and/or selectivity, an atomic level understanding of the RuO_2/water interface is of fundamental importance.

The electrochemical behavior of RuO_2 has now been studied for a significant period of time, ever since the early 1970s when Trasatti reported its potential as an electrode material based on the results of electrochemical measurements.[19] As techniques for the preparation and assessment of single crystals have improved, the behavior of electrodes with typical surface orientations has been elucidated, and features of the electrocatalytic activity and charging/discharging processes have been disclosed.[8,20–27] These processes have been investigated by Doblhofer et al. by measuring the amount of charge transferred, and estimating the valency of surface Ru during the charging/discharging processes.[20] Reaction mechanisms and trends in the catalytic activity have also been studied and explained using density functional theory (DFT), although these studies have neglected the effect of the electrolyte on the electrode interface.[28–30] The atomic-scale interfacial structure was studied by Nagy and coworkers[24,31] using surface X-ray diffraction measurements, and this work represented an important step toward a fundamental understanding of interfacial phenomena. In general, it is very challenging to study atomic-scale phenomena at the interface because of the complexity of the electrochemical environment. Efforts to reveal these phenomena therefore require both experimental observations and ab initio calculations.

Generally, the electrocatalytic activity depends on the electrochemical conditions. Benchmark experiments focusing on the oxygen evolution reaction (OER) were reported by Shao-Horn et al.[6,8] These studies examined differences in onset potential at a single crystal $RuO_2(110)$ surface under acidic and basic conditions and at high current density under acidic conditions, using potential-current density plots.[6] It has also been found that the OER over RuO_2 has two distinct Tafel slopes, below and above 1.5 V vs. RHE.[6,8] DFT calculations have shown that the change in the Tafel slope is caused by a transition of the rate-determining step from de-hydrogenation to an O-O coupling process.[32] From these experimental and theoretical studies, it is evident that both the atomic-scale interfacial structure and the reaction itself are greatly affected by the electrochemical conditions. Therefore, the purpose of the present study was to investigate the atomic-scale structure of the RuO_2/water interface by DFT calculations, taking into account the pH and electrode potential.

There are several well-established methods that can be used to investigate electrochemical reactions based on DFT calculations. One example is the computational hydrogen electrode, which includes the chemical potential of the H^+ + e^- pair by relating it to a reversible hydrogen electrode (RHE) reference.[33] A scheme that considers the electrode potential and pH separately was recently reported and applied to a Pt(111)/water system.[34] In brief, this scheme relies on varying the orientation of water molecules as well as the hydrogen concentration at the interface. In this Chapter, this technique was applied to the RuO_2/water system to examine the role of the electrode potential and pH on the interface structure.

5.2 **Method**

First principles calculations including the effects of pH and electrode potential were performed to analyze the structure of the RuO_2/water interface by using the method introduced in section 2.2.2. where interfacial Gibbs energy can be defined as a function of pH and electrode potential separately,

$$\begin{aligned} G_{int}(\mu_{\mathrm{H}^++e^-}, \Phi_{e^-}) &= G_{int}(\mu_{\mathrm{H}^++e^-} = 0, \Phi_{e^-}) - \frac{n}{N}\mu_{\mathrm{H}^++e^-} \\ \mu_{\mathrm{H}^++e^-} &= \Phi_{e^-}(\mathrm{SHE}) - 2.3k_BT \cdot \mathrm{pH} - \Phi_{e^-} \\ &= -eU_{SHE} - 2.3k_BT \cdot \mathrm{pH}\,. \end{aligned} \tag{5.1}$$

In these calculations, $\Phi_{e^-}(\mathrm{SHE})$ is set to 4.6 eV. Using DFT calculations, the Gibbs free energies of the RuO_2/water interface ($G_{N,n}$, $G_{N,0}$) can be estimated directly from the results of total energy calculations including thermal corrections. The use of $G_{\mathrm{int}}(\mu_{\mathrm{H}^++e^-}, \Phi_{e^-})$ enables us to include the effects of dipoles at the interface and hence explicitly account for the influence of the electric field. Consequently, the interfacial structures can be obtained by separately investigating pH and electrode potential. It should be stressed that all potential counter-ions, except protons, have been ignored in the present study. A means of systematically including more ions has already been proposed;[35] however, such rigorous analysis would increase the number of DFT calculations by at least an order of magnitude.

A $RuO_2(110)$ facet was selected as a model of the RuO_2/water interface because the existence of this facet has been demonstrated by nanoparticle XRD analyses[6] and since it has been determined to possess the lowest surface energy by DFT calculations.[36] A RuO_2/water interface structure without protons was used as a reference system. Figure 5-1 shows the unit cell of the reference system, which contains four surface oxygen atoms, two of which are labelled as “br” (for bridge site) and two as “cus” (for coordinatively unsaturated site). Other possible interfacial structures can be modeled by changing the state of the surface native O to –O, -OH or $–H_2O$; that is, by varying the formal valence of the surface Ru atoms. In the following discussion, the notation X^{br}/X^{cus} (X = O, OH, H_2O) is used to indicate the ratios of various oxygen states at the “br” and “cus” sites. The term n/N is used to denote the coverage of surface oxygen species by hydrogen as a means of classifying the interfacial structures:

$n/N = 0.0$ (such as O^{cus}/O^{br}),
$n/N = 0.5$ (OH^{cus}/O^{br}, O^{cus}/OH^{br}),
$n/N = 1.0$ (OH^{cus}/OH^{br}, H_2O^{cus}/O^{br}, O^{cus}/H_2O^{br}),
$n/N = 1.5$ (H_2O^{cus}/OH^{br}, OH^{cus}/H_2O^{br}) and
$n/N = 2.0$ (H_2O^{cus}/H_2O^{br}),

where n is the number of hydrogen atoms and N is the number of surface oxygen atoms (N=4). Interfacial structures with n=0,2,4,6, and 8 have been included in our calculations. A selection of the interfacial structures associated with the various n/N ratios are shown in Figure 5-2. When the system contained water (H_2O^{cus} or H_2O^{br}), the orientations of the water molecules were varied such that they were positioned either facing up (with the protons pointing out from the surface), parallel or down (with the protons pointing toward the surface). In the case of n/N=0.0, molecularly adsorbed oxygen was also considered. In this manner, more than 60 configurations were modeled and $G_{\text{int}}\left(\mu_{\text{H}^{+}+e^{-}} = 0, \Phi_{e^{-}}\right)$(abbr.$G_{\text{int}}^{0}$), $G_{\text{int}}\left(\mu_{\text{H}^{+}+e^{-}}, \Phi_{e^{-}}\right)$ (abbr. G_{int}) and $\Phi_{e^{-}}$ were calculated based on these models. In addition, the configurations having lower G_{int}^{0} values were selected and two water layers were added to include the effects of water affinity and orientation. To model a water layer, a square structure was introduced, forming a hydrogen network with four surface oxygen atoms in the unit cell. The orientation of the first water layer was varied in three ways as illustrated below:

$$(\text{i})\ \begin{matrix} \text{u} & \cdots & \text{p} \\ \vdots & & \vdots \\ \text{p} & \cdots & \text{u} \end{matrix} \qquad (\text{ii})\ \begin{matrix} \text{u} & \cdots & \text{p} \\ \vdots & & \vdots \\ \text{p} & \cdots & \text{d} \end{matrix} \qquad (\text{iii})\ \begin{matrix} \text{d} & \cdots & \text{p} \\ \vdots & & \vdots, \\ \text{p} & \cdots & \text{d} \end{matrix}$$

where ‘u,’ ‘p’ and ‘d’ indicate up, parallel and down orientations. The second water layer was fixed in configuration (ii). A total of 36 of these water-enriched structures were considered, meaning that a total of almost 100 configurations were modeled in the present study.

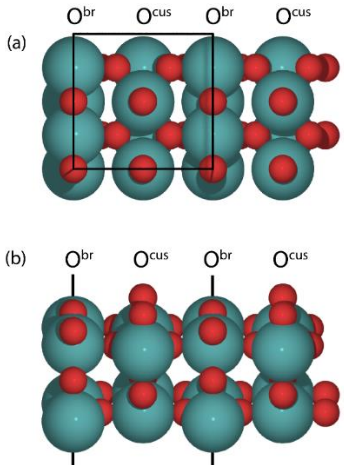

Figure 5-1. Reference system for the RuO_2(110)/water interface: (a) top view and (b) side view (only the two topmost surface layers are shown). Red balls represent oxygen atoms and green balls represent ruthenium atoms. The surface contains two different types of oxygen atoms: O^{br} (bridging oxygen atom) and O^{cus} (coordinatively

unsaturated oxygen atom).

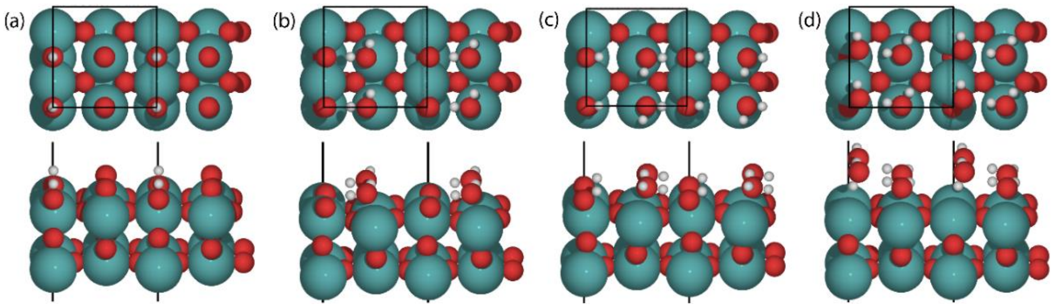

Figure 5-2. Top view (upper row) and side view (lower row) of select $RuO_2(110)$/water interface structures: (a) n/N = 0.5 (b) n/N = 1.0 (c) n/N = 1.5 (d) n/N = 2.0

This method requires as input a set of probable interfacial structures, and the accuracy of the resulting predictions will depend on the completeness of the set. Hence, in order to include the total energy and work function of as many configurations as possible, all the structures generated during the geometry optimization were included. Figure 5-3 illustrates one of the energy minimization processes, including the changes in work function and water orientation. During the geometry optimization, the total energy becomes smaller and smaller and the water orientation transitions to parallel. At the same time, the corresponding work function varies from 3.2 to 4.6 eV. If one focuses on the last four steps of the optimization, the work function is seen to drop by 0.41 eV while the total energy remains relatively constant (within 0.11 eV). Thus, incorporating the non-optimized structures enables the inclusion of a wide range of work function values despite small variations in the total energy, which is required to ensure completeness of the set. For this reason, the results from non-optimized structures were included in the set.

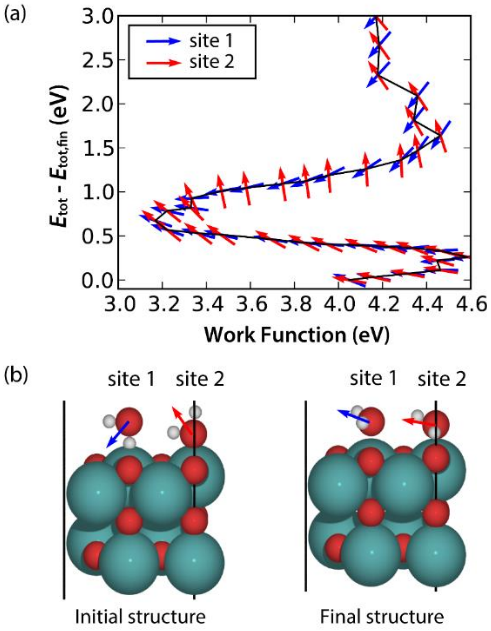

Figure 5-3. Change in total energy, work function and water orientation (surface dipole) during geometry optimization. (a) Illustration of the optimization process in terms of a relative total energy vs. work function plot. Blue and red arrows indicate the water orientations on site 1 and site 2, respectively. (b) Initial and final structures during the geometry optimization.

5.3 Results and discussion

5.3.1 Interfacial Gibbs energy and surface Pourbaix diagram

Interfacial Gibbs energies were calculated as functions of both pH and electrode potential, and the results are summarized in Figure 5-4. Here, each point corresponds to one interfacial structure. The point with the lowest G_{int} at a given electrode potential is the most stable interfacial structure at that potential and pH. At negative electrode potentials, each surface oxygen is bonded to two hydrogen atoms as water. With increasing potential, the surface hydrogen atoms tend to desorb and, at approximately 2.0 V vs. RHE, hydrogen is no longer present on the surface oxygen. This general electrochemical behavior and the features of the electrochemical interface are reproduced by DFT calculations if both dissolution and phase transition of the bulk system are ignored. Figure 5-4 presents structures with and without water layers, indicated by solid and semi-transparent symbols, respectively. The structures with water layers are in general more stable, reflecting the fact that the addition and removal of hydrogen atoms from surface oxygen are energetically more favorable in the presence of water than without.

The most stable interfacial structures at different pH and electrode potential values are shown in the surface Pourbaix diagram in Figure 5-5. This diagram was obtained by selecting the most stable structures at 0.2 V intervals. Our results indicate that the most dominant surface states are n/N = 1.0, 0.5 and 0.0 in the ranges of 0.0 – 1.1, 1.1 – 1.5 and above 1.5 V vs. RHE, respectively. Here, n/N values of 0.0, 0.5, 1.0, 1.5 and 2.0 are, on average, equivalent to a formal surface Ru valency of 5.0, 4.5, 4.0, 3.5 and 3.0. Therefore, in our simulations, Ru(IV), Ru(IV/V) and Ru(V) are present at 0.4, 1.0 and 1.4 V vs. RHE, respectively, at pH 0. Based on their experimental results, Doblhofer et al.[20] suggested that Ru(III), Ru(IV) and Ru(V) are present at approximately these same voltage. Thus, there is reasonable agreement between our simulations and the experimental data, although the exact potentials at which the surface oxidation states change differ slightly. It should be noted that the simulation of the interfacial structures was limited by the range of n/N values employed, the ambiguity in the value of the $\Phi_{e^-}(\mathrm{SHE})$ term and by the accuracy of the work function. Hence, it was difficult to obtain a perfect match between theoretical and experimental values. We further note the importance of pKa. Evaluation of pKa would extend the Pourbaix diagram so as to include information about stable charged systems.[44] However, these do not feature in our study because calculations on charged systems require corrections in the implementation of the periodic boundary conditions.

In the potential range above 0.4 V vs. RHE, where experimental structures are stable,[26] there is reasonable agreement between the generated interfacial structures and experimental data. At pH = 0, O^{br}/H_2O^{cus} was found to dominate between 0.4 and 1.1 V vs. RHE, $O^{br}/0.5H_2O^{cus}$ between 1.1 and 1.5 V vs. RHE and O^{br}/O^{cus} above 1.5 V vs. RHE. Here, $0.5H_2O^{cus}$ indicates that half of the O^{cus} atoms were bound to two hydrogen atoms. Interestingly, so-called non-Nernstian behavior was observed between n/N = 0.0/0.5 and n/N = 1.0/1.5. That is, the n/N border did not exhibit a Nernstian slope of 59 mV/pH. The reason for this behavior is discussed in Chapter 5.3.2. In addition, the large differences identified with respect to the interfacial structure in the n/N = 0.0 region are addressed in Chapter 5.3.3.

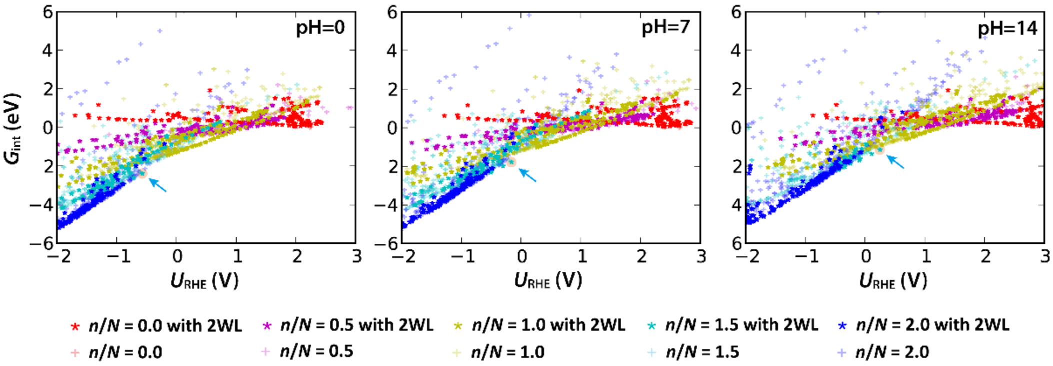

Figure 5-4 Calculated interfacial Gibbs energy vs. electrode potential at pH=0 (left), pH=7 (center) and pH=14 (right). The electrode potential is scaled to RHE. The solid symbols correspond to structures with water layers while semi-transparent symbols correspond to structures without water layers. The red, purple, yellow, light blue, and blue symbols represent coverages of 0.0, 0.5, 1.0, 1.5 and 2.0.

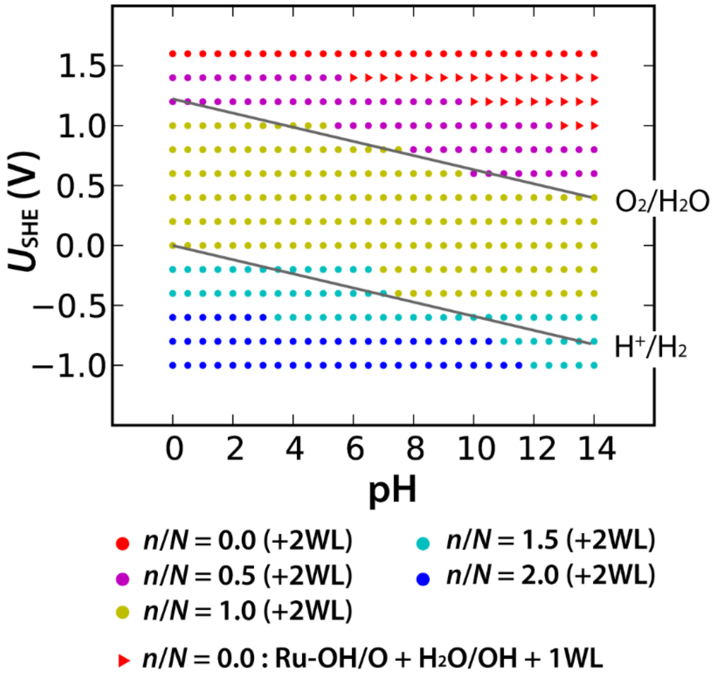

Figure 5-5 Surface Pourbaix diagram for RuO_2(110). The colors correspond to the hydrogen coverages listed below the diagram. Gray lines indicate the redox potential of O_2/H_2O and H^+/H_2. Red triangles found in the n/N = 0.0 region represent structures that contain OH^{br}/O^{cus} at the surface, OH/H_2O molecules in the first electrolyte layer and H_2O molecules in the second layer.

5.3.2 Structural feature at the RuO_2/water interface

One striking feature of the RuO_2/water interface is its non-Nernstian behavior, meaning that the slope of the electrode potential plotted against pH does not have a value of 59 mV/pH. This result indicates that the formal valency of the surface Ru exhibits pH dependence at a constant RHE potential. In a previous cyclic voltammetry analysis of RuO_2(110) single crystals,[26] three peaks (at 0.75, 0.92 and 1.26 V) were observed in acidic media. In contrast, the first two peaks were found to merge under basic conditions, leaving only two peaks (around 1.0 V and above 1.4 V).

Although the merging of these two peaks as the pH is increased could not be observed in our study because of the limited number of distinct atomic models and the neutrality of the system, the anodic shift around the OER potential region could be reproduced in our calculations.

This non-Nernstian behavior originates from two characteristics of the interface. The first is a particularly stable interfacial structure. As an example, the slope between $n/N = 1.5$ and 1.0 is less than the Nernstian value, due to the presence of a stable hydrogen network. Because of the particular lattice constant of RuO_2, the distance between surface oxygen atoms is suitable for the formation of a hydrogen network. As such, one interfacial structure having a stable hydrogen network was identified, as indicated by the arrows in Figure 5-4. Normally, structures with lower n/N values become more stable as the potential increases because of the smaller quantity of H^++e^- pairs, which are destabilized by the potential increase. However, in the present case, the increased destabilization, which is proportional to n/N, is compensated for by the formation of a stable hydrogen network. Thus, the structure with $n/N = 1.5$ is found in the higher potential region under basic conditions.

Another reason for the observed non-Nernstian behavior is the dependence of G_{int}^{0} on $\Phi_{e\text{-}}$ that results from the dipole-field interaction at $\mu_{\mathrm{H}^{+}+e^{-}} = 0$. In a previous study of Pt(111), the effect of the field on the adsorption energy of reaction intermediates was found to be non-negligible because of the interaction between the dipoles of the adsorbates and the electric field.[45] For similar reasons, G_{int}^{0} is somewhat affected by $\Phi_{e\text{-}}$ in our systems and as a result the slope of G_{int} vs. U_{RHE} is no longer equal to n/N. This is observed between $n/N = 0.0$ and 0.5; a plot of G_{int} at $n/N = 0$ shows a small negative slope even though the term $n/N\mu_{\mathrm{H}^{+}+e^{-}}$ is always zero over this region. As a result, the change from $n/N = 0.5$ to 0.0 occurred at approximately $U_{\mathrm{RHE}} = 1.5$ V at pH 0 but at $U_{\mathrm{RHE}} = 1.7$ V at pH 14. This trend could explain the differences observed for the OER under acidic and basic conditions. Previous DFT calculations have shown that variations in surface structure cause changes in the rate determining step,[32] which could give rise to the change in the Tafel slope at approximately 1.5 V vs. RHE. The results of our calculations demonstrate that, in the vicinity of 1.5 V, the interfacial structure changes from one that has a minimal quantity of hydrogen atoms bonded to surface oxygen to one in which no hydrogen is present at the interface. In particular, a structural change occurs at 1.5 V when applying acidic conditions and at 1.7 V under basic conditions. Previous experimental work has determined that the Tafel slope changes at a slightly higher point in basic media (1.51 V vs. RHE) than in acidic (1.48 V vs. RHE).[6] Thus, our results are consistent with those of previous studies and, in addition, explain the origin of the potential difference.

5.3.3 Origin of structural differences between pH 0 and 14 in the OER region

A significant structural difference was found between pH values of 0 and 14 in the OER potential region (1.6 V vs. RHE at pH 0 and 1.8 V vs. RHE at pH 14). The surface structure at pH 0 is O^{br}/O^{cus} as shown in Figure 5-6 (a), while the surface at pH 14 is OH^{br}/O^{cus} with a water layer consisting of OH/H_2O as shown in Figure 5-6 (b). Although the values of n/N are the same in both models, the water layer geometries and the formal valencies of the surface Ru are quite different. This variation account for the observed pH-dependent behavior of the OER, either through a change in the mechanism or a variation in the most probable initial reactions. In this respect, it is helpful to discuss the origin of the pH-dependent interfacial structure with regard to the work function. The work function difference between pH 0 and 14 is 0.84 eV at the same RHE potential, and so the structure having the smaller work function is always obtained under the basic conditions. For this same reason, in the case of the Pt(111)/water interface, the orientation of water molecules tends to change from H-down to H-up as the pH increases.[34] In the present study, work function values of 6.3 and 5.7 eV, respectively, were obtained at pH 0 (1.6 V vs. RHE) and pH 14 (1.8 V vs. RHE) as shown in Figure 5-7. In order to clarify the origin of these different work functions, we divided the system into three regions: RuO_2 (region I), the first water (or OH) layer (region II) and the second water layer (region III), also shown in Figure 5-7. The work functions in region I are 6.86 eV at pH 0 and 5.06 eV at pH 14. Although the work function was reduced when the dipoles of the water in region II at pH 0 had a H-up orientation (work function of region I + region II = 6.18 eV) and was increased when the dipoles of the OH/water in region II at a pH of 14 were oriented H-down (work function of region I + region II = 5.44 eV), the large difference in the work function in region I was not completely screened by the outer water layer. This phenomenon seems to be typical of transition metal oxides in which surface metal atoms can have several formal valency values.

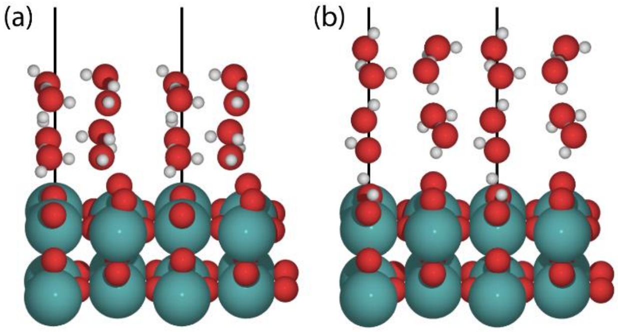

Figure 5-6 Simulated interfacial structure of RuO_2(110); (a) U_{RHE} = 1.6 V, pH=0 (b) U_{RHE} = 1.8 V, pH=14

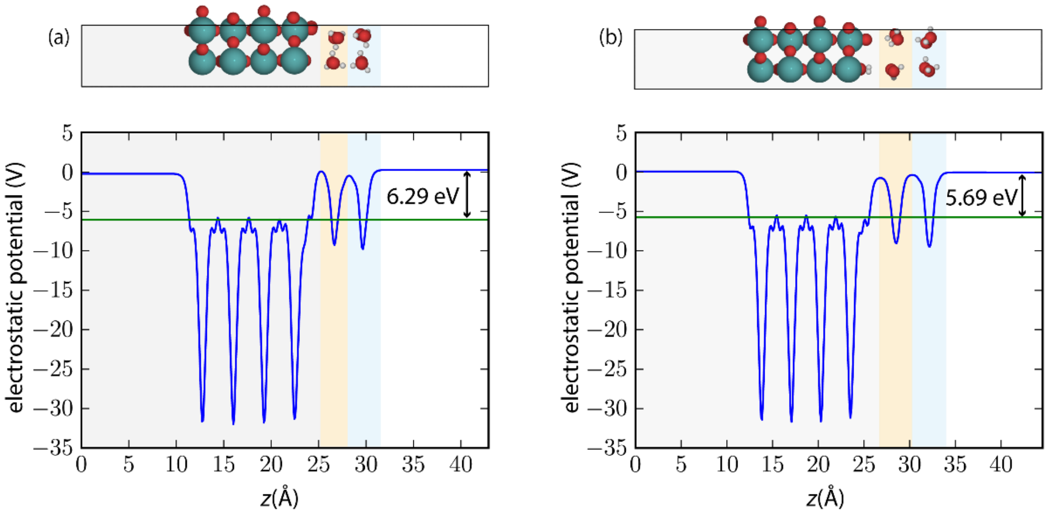

Figure 5-7 Electrostatic potential distribution throughout an interface and side view of the corresponding structure. (a) U_{RHE} = 1.6 V, pH=0 and (b) U_{RHE} = 1.8 V, pH=14. Three distinct regions have been marked: RuO_2 (region I, gray), 1st water bi-layer (region II, yellow) and 2nd water bi-layer (region III, blue).

In summary, as pH increases, interfaces with lower work functions will be generated at a given electrode potential vs. RHE. The interface between the metal oxide and water includes many polarizable molecules and adsorbates, such as water, O* and OH*. The orientations of these species change with pH in accordance with the requirements imposed by the Born-Haber cycle. Thus, transition states can also depend on pH, especially those of polarizable processes such as proton transfer. This is to some extent verified by the finding that the differences in current density under acidic and basic conditions are primarily observed below 1.5 V vs. RHE,[6] the potential region in which proton transfer is believed to be the rate-determining step.[32] Although the transition states under constant electrode potential and pH have not been determined, we believe that differences in orientations can contribute to the pH-dependent OER activity.

5.4 Conclusions

First-principles calculations that account for the effects of pH and electrode potential were performed to analyze the structure of the electrochemical RuO_2/water interface. A new scheme to accurately treat the chemical potentials of protons and electrons enabled an assessment of the interfacial Gibbs energy as a function of both pH and electrode potential. The results were reported in a surface Pourbaix diagram that provided a visual representation of the pH and potential dependence of the interfacial structures. At pH 0, the predicted interfacial structures consisted of O^{br}/H_2O^{cus} (0.4-1.1 V vs. RHE), $O^{br}/0.5H_2O^{cus}$ (1.1-1.5 V vs. RHE) and O^{br}/O^{cus} (above 1.5 V vs. RHE). A comparison between pH values of 0 and 14 revealed two interesting features. Firstly, the slope between certain n/N values did not exhibit the expected Nernstian value, a clear manifestation of non-Nernstian behavior. This feature could be attributed to a stable hydrogen network and the effect of the electric field on the binding energy of the adsorbates. The second feature was the structural difference within the $n/N = 0.0$ region, resulting from the decrease in work function that accompanies an increase in pH. The reduction in the work function may be ascribed to either the H-up orientation of water molecules relative to the interface or to a decrease in the formal valency of surface Ru atoms. Finally, we note that the method applied in the present study is well-suited to the estimation of the effects of both pH and electrode potential on the structure of an electrochemical interface. However, because of limitations in the atomic model employed and the accuracy of the calculations, there is still a gap between this type of atomic-scale investigation and actual electrochemical systems. Additionally, a scheme capable of examining the effects of pH and electrode potential on barriers and kinetics is still missing. Overcoming these challenges will represent the next step toward modeling and designing electrochemical interfaces for specific reactions.

References

(1) Exner, K. S.; Anton, J.; Jacob, T.; Over, H. *Angew. Chemie Int. Ed.* 2014, **53**, 11032.

(2) Exner, K. S.; Anton, J.; Jacob, T.; Over, H. *Electrochim. Acta* 2014, **120**, 460.

(3) Over, H. *J. Phys. Chem. C* 2012, **116**, 6779.

(4) Zweidinger, S.; Crihan, D.; Knapp, M.; Hofmann, J. P.; Seitsonen, A. P.; Weststrate, C. J.; Lundgren, E.; Andersen, J. N.; Over, H. *J. Phys. Chem. C* 2008, **112**, 9966.

(5) Seitsonen, A. P.; Over, H. *J. Phys. Chem. C* 2010, **114**, 22624.

(6) Lee, Y.; Suntivich, J.; May, K. J.; Perry, E. E.; Shao-Horn, Y. *J. Phys. Chem. Lett.* 2012, **3**, 399.

(7) Lyons, M. E. G.; Floquet, S. *Phys. Chem. Chem. Phys.* 2011, **13**, 5314.

(8) Stoerzinger, K. A.; Qiao, L.; Biegalski, M. D.; Shao-Horn, Y. *J. Phys. Chem. Lett.* 2014, **5**, 1636.

(9) Silva, L. M. Da; Boodts, J. F. C.; De Faria, L. A. *Electrochim. Acta* 2001, **46**, 1369.

(10) Spataru, N.; Tokuhiro, K.; Terashima, C.; Rao, T. N.; Fujishima, A. *J. Appl. Electrochem.* 2003, **33**, 1205.

(11) Qu, J.; Zhang, X.; Wang, Y.; Xie, C. *Electrochim. Acta* 2005, **50**, 3576.

(12) Chang, K. H.; Hu, C. C.; Chou, C. Y. *Electrochim. Acta* 2009, **54**, 978.

(13) Deshmukh, P. R.; Pusawale, S. N.; Jagadale, A. D.; Lokhande, C. D. *J. Mater. Sci.* 2012, **47**, 1546.

(14) Rochefort, D.; Pont, A. L. *Electrochem. commun.* 2006, **8**, 1539.

(15) Kötz, R.; Kötz, R.; Carlen, M.; Carlen, M. *Electrochim. Acta* 2000, **45**, 2483.

(16) Zheng, J. P. *J. Electrochem. Soc.* 1995, **142**, 2699.

(17) Hu, Y.-Y.; Liu, Z.; Nam, K.-W.; Borkiewicz, O. J.; Cheng, J.; Hua, X.; Dunstan, M. T.; Yu, X.; Wiaderek, K. M.; Du, L.-S.; Chapman, K. W.; Chupas, P. J.; Yang, X.-Q.; Grey, C. P. *Nat. Mater.* 2013, **12**, 1130.

(18) Chang, K. H.; Hu, C. C.; Chou, C. Y. *Chem. Mater.* 2007, **19**, 2112.

(19) Trasatti, S.; Buzzanca, G. *J. Electroanal. Chem. Interfacial Electrochem.* ***1971***, **29**, A1.

(20) Doblhofer, K.; Metikos, M.; Ogumi, Z.; Gerischer, H. *Ber. Bunsengess. Phys. Chem.* 1978, **82**, 1046.

(21) Castelli, P.; Trasatti, S. *J. Electroanal. Chem.* 1986, **210**, 189.

(22) Over, H. *Science.* 2000, **287**, 1474.

(23) Kim, Y. D.; Seitsonen, A. P.; Wendt, S.; Wang, J.; Fan, C.; Jacobi, K.; Over, H.; Ertl, G. *J. Phys. Chem. B* 2001, **105**, 3752.

(24) Lister, T. E.; Chu, Y.; Cullen, W.; You, H.; Yonco, R. M.; Mitchell, J. F.; Nagy, Z. *J. Electroanal. Chem.* 2002, **524-525**, 201.

(25) Doubova, L. M.; Daolio, S.; Battisti, A. De; Doubo, L. M. *J. Electroanal. Chem.* 2002, **532**, 25.

(26) Guerrini, E.; Consonni, V.; Trasatti, S. *J. Solid State Electrochem.* 2005, **9**, 320.

(27) Juodkazis, K.; Juodkazytė, J.; Šukienė, V.; Grigucevičienė, A.; Selskis, A. *J. Solid State Electrochem.* 2008, **12**, 1399.

(28) Rossmeisl, J.; Qu, Z. W.; Zhu, H.; Kroes, G. J.; Nørskov, J. K. *J. Electroanal. Chem.* 2007, **607**, 83.

(29) Man, I. C.; Su, H.-Y.; Calle-Vallejo, F.; Hansen, H. a.; Martínez, J. I.; Inoglu, N. G.; Kitchin, J.; Jaramillo, T. F.; Nørskov, J. K.; Rossmeisl, J. *ChemCatChem* 2011, **3**, 1159.

(30) Halck, N. B.; Petrykin, V.; Krtil, P.; Rossmeisl, J. *Phys. Chem. Chem. Phys.* 2014, **16**, 13682.

(31) Chu, Y. S.; Lister, T. E.; Cullen, W. G.; You, H.; Nagy, Z. *Phys. Rev. Lett.* 2001, **86**, 3364.

(32) Fang, Y.-H.; Liu, Z.-P. *J. Am. Chem. Soc.* 2010, **132**, 18214.

(33) Nørskov, J. K.; Rossmeisl, J.; Logadottir, A.; Lindqvist, L.; Kitchin, J. R.; Bligaard, T.; Jónsson, H. *J. Phys. Chem. B* 2004, **108**, 17886.

(34) Rossmeisl, J.; Chan, K.; Ahmed, R.; Tripković, V.; Björketun, M. E. *Phys. Chem. Chem. Phys.* 2013, **15**, 10321.

(35) Nielsen, M.; Björketun, M. E.; Hansen, M. H.; Rossmeisl, J. *Surf. Sci.* 2015, **631**, 2.

(36) Xu, C.; Jiang, Y.; Yi, D.; Zhang, H.; Peng, S.; Liang, J. *J. Am. Ceram. Soc.* 2014, **97**, 3702.

(37) Mortensen, J. J.; Hansen, L. B.; Jacobsen, K. W. *Phys. Rev. B.* 2005, **71**, 1.

(38) Enkovaara, J.; Rostgaard, C.; Mortensen, J. J.; Chen, J.; Dułak, M.; Ferrighi, L.; Gavnholt, J.; Glinsvad, C.; Haikola, V.; Hansen, H. A.; Kristoffersen, H. H.; Kuisma, M.; Larsen, A. H.; Lehtovaara, L.; Ljungberg, M.; Lopez-Acevedo, O.; Moses, P. G.; Ojanen, J.; Olsen, T.; Petzold, V.; Romero, N. A.; Stausholm-Møller, J.; Strange, M.; Tritsaris, G. A.; Vanin, M.; Walter, M.; Hammer, B.; Häkkinen, H.; Madsen, G. K. H.; Nieminen, R. M.; Nørskov, J. K.; Puska, M.; Rantala, T. T.; Schiøtz, J.; Thygesen, K. S.; Jacobsen, K. W. *J. Phys. Condens. Matter* 2010, **22**, 253202.

(39) Bahn, S. R.; Jacobsen, K. W. *Comput. Sci. Eng.* 2002, **4**, 56.

(40) Hammer, B.; Hansen, L.; Nørskov, J. *Phys. Rev. B* 1999, **59**, 7413.

(41) Blöchl, P. E. *Phys. Rev. B* 1994, **50**, 17953.

(42) Boman, C.-E.; Danielsen, J.; Haaland, A.; Jerslev, B.; Schäffer, C. E.; Sunde, E.; Sørensen, N. A. Refinement of the Crystal Structure of Ruthenium Dioxide. *Acta Chemica Scandinavica*, 1970, **24**, 116.

(43) Monkhorst, H. J.; Pack, J. D. *Phys. Rev. B* 1976, **13**, 5188.

(44) Marenich, A. V.; Majumdar, A.; Lenz, M.; Cramer, C. J.; Truhlar, D. G. *Angew. Chemie - Int. Ed.* 2012, **51**, 12810.

(45) Karlberg, G. S.; Rossmeisl, J.; Nørskov, J. K. *Phys. Chem. Chem. Phys.* 2007, **9**, 5158.

Chapter 6

Concluding Remarks

In my thesis, oxygen reduction and evolution reactions are examined by means of DFT with the concept of local active site modification, addressing an electron/hole transfer across the interface, and bridging simulation model and electrochemical environment. In Chapter 3, a kinetics of oxygen reduction reaction on Ta_3N_5 is investigated and effect of defects are discussed. I show impurity states are origin of the activity because an initial step of the reaction i.e. oxygen adsorption, is triggered by an electron transfer from impurity states of semiconductor to π^* orbital of oxygen molecule. The calculation model is simple that contains minimum water molecules and energy dependence on electrode potential is evaluated as a means of simple computational hydrogen electrode method. In Chapter 4, thermodynamics of hole transfer on oxygen evolution reaction is investigated by interfacial band diagrams of Ta_3N_5/water. I get a one-to-one correspondence between electrode potential and band diagram including Schottky barrier height. The Schottky barrier is not a simple function of electrode potential because either band edge pinning, Fermi level pinning, or simple Fermi level reduction is dominant according to the potential region. The model in Chapter 4 is more realistic than that in Chapter 3 in that it includes explicit water molecules and electrode potential of the system is measured by its work function. In Chapter 5, the structure of the RuO_2/water interface was examined over a range of pH and electrode potential values. A new scheme to accurately treat the chemical potentials of protons and electrons enabled an assessment of the interfacial Gibbs energy as functions of both pH and electrode potential. As pH increases, interfaces with lower work function is generated at a given electrode potential in accordance with the requirements imposed by the Born-Haber cycle. The interface of metal oxide/water includes many polarizable molecules and adsorbents such as water, O* and OH*, and orientations of these differ by pH. I suppose pH dependent activity of oxygen evolution reaction is possibly originated from such difference because it has significant impact on kinetics. Throughout my thesis, I show the strategy to improve electrocatalytic activities of oxygen reduction reaction and oxygen evolution reaction. Now I remark the challenges toward more realistic i.e. 'in situ' simulations of electrocatalysts. A first challenge is bridging the remaining gaps between simulations and experiments. For example, only limited number of ions can be included explicitly, however, a number of them should be included for the description of electric double layer. A second challenge is kinetics. Searching transition states under constant electrode potential are achieved only on a small cluster. Moreover, revealing kinetics on the electrochemical system including effects of electrode potential, pH, and ions together are rather difficult.

In conclusion, toward the computational design of electrocatalysts, highly accurate calculations are needed for the prediction of electrode potential, surface geometry and reactions as well as large scale calculations for complex system in order to overcome the challenges. In addition, how to model "chemistry" is remarkably important. It is almost impossible to simulate the whole system including ~10^{23} atoms. Extracting essential aspects of complex chemistry requires information or intuitions about the determining factors in reactions. I believe that the combination of experiments and first-principles calculations will help provide the factors. Uncovering electrochemical reactions in various experimental conditions by means of first principles calculations will offer valuable clues that cannot be unveiled by either of them alone. Achieving the computational design of electrocatalysts is significantly challenging but still worthwhile to advance the state-of-the-art materials science.

Publications stemming from this work

1. E. Watanabe, H. Ushiyama and K. Yamashita,

"Theoretical studies on the stabilities and reactivities of Ta_3N_5 (100) surfaces",

Chem. Phys. Lett. **561**, 57 (2013).

2. E. Watanabe, H. Ushiyama and K. Yamashita,

"Theoretical studies on the mechanism of oxygen reduction reaction on clean and O-substituted Ta_3N_5(100) surfaces",

Catal. Sci. Technol. **5**, 2769 (2015).

3. E. Watanabe, J. Rossmeisl, M. E. Björketun, H. Ushiyama, K. Yamashita,

“Atomic-scale analysis of the RuO_2/water interface under electro-chemical conditions”, submitted.

4. E. Watanabe, H. Ushiyama and K. Yamashita,

“Interfacial structure and band alignment of n-type Ta_3N_5/water for photoelectrochemical water oxidation”, in preparation.